PFC/JA-84-38

COLLECTIVE INSTABILITIES DRIVEN BY ANODE PLASMA IONS AND ELECTRONS IN A NONRELATIVISTIC CYLINDRICAL DIODE WITH APPLIED MAGNETIC FIELD

Ronald C. Davidson
Kang T. Tsang
Han S. Uhm

October, 1984

COLLECTIVE INSTABILITIES DRIVEN BY ANODE PLASMA IONS AND ELECTRONS IN A NONRELATIVISTIC CYLINDRICAL DIODE WITH APPLIED MAGNETIC FIELD

Ronald C. Davidson
Plasma Fusion Center
Massachusetts Institute of Technology, Cambridge, MA 02139

Kang T. Tsang
Science Applications Inc., Boulder, CO 80302

Han S. Uhm
Naval Surface Weapons Center, Silver Spring, MD 20910

ABSTRACT

Use is made of the macroscopic cold-fluid-Poisson equations to investigate the electrostatic stability properties of nonrelativistic, nonneutral electron flow in a cylindrical diode with applied magnetic field $B_0\hat{e}_z$. The cathode is located at r=a and the anode is located at r=b. Space-charge-limited flow with $E_r^0(r=a)=0$ is assumed. Detailed stability properties are investigated analytically and numerically for electrostatic flute perturbations with $\partial/\partial z=0$. Particular emphasis is placed on the influence of neutral anode plasma on stability behavior assuming uniform cathode electron density ($\hat{n}_b$) extending from the cathode (r=a) to $r=r_b$, and uniform anode plasma density ($\hat{n}_e=Z_i\hat{n}_i$) extending from $r=r_p$ to the anode (r=b). Depending on the cathode electron density (as measured by $s_b=\hat{\omega}_{pb}^2/\omega_{ce}^2$), the anode plasma density (as measured by $s_e=\hat{\omega}_{pe}^2/\omega_{ce}^2$), the diode aspect ratio, etc., it is found that there can be a strong coupling of the anode plasma to the cathode electrons, and a concomitant large influence on detailed stability behavior for both the high-frequency (electron-driven) and low-frequency (ion-driven) branches. Detailed stability properties are investigated over a wide range of cathode electron density, anode plasma density, diode aspect ratio, etc.

I. INTRODUCTION AND SUMMARY

There is a growing literature on the equilibrium and linear stability properties of sheared, nonneutral electron flow in cylindrical[1] and planar[2-6] models of high-voltage diodes with application to the generation of intense charged particle beams for inertial confinement fusion.[7] These analyses[1-6] have represented major extensions of earlier work[8-11] to include the important influence of cylindrical,[1] relativistic,[2-6] electromagnetic[2-6] and kinetic[6] effects on stability behavior at moderately high electron density. However, none of these treatments[1-6] has included the influence of active plasma components in the anode-cathode gap. Indeed, it would be expected that plasma ions and electrons could interact effectively with the cathode electrons and modify stability behavior. For example, it is well established in applications related to heavy ion accelerators[12-14] and electron ring accelerators[15] and in basic theoretical studies[16-19] of nonneutral plasma stability properties that the collective interactions associated with an active ion component in an electron-rich background can lead to an instability known as the ion resonance instability.[12] The strength of the ion resonance instability depends on a number of factors, including ion density, the relative motion of electron and ion components, and the strength of the equilibrium self electric fields. As such an instability may have deleterious effects on stable diode operation and/or the production of well-collimated ion beams, one purpose of the present analysis is to investigate detailed properties of the ion resonance instability in geometry particular to cylindrical diodes (Fig. 1). In addition, we investigate the stability behavior associated with the (high-frequency) interaction of the plasma electrons with the cathode electrons.

In the present analysis, we make use of a macroscopic, cold-fluid model to investigate the electrostatic equilibrium and stability properties of nonrelativistic nonneutral plasma in a cylindrical diode with applied magnetic field $B_0\hat{\underset{\sim}{e}}_z$. As illustrated in Fig. 1, the cathode is located at r=a and the anode at r=b, and space-charge-limited flow with $E_r^0(r=a)=0$ is assumed. In general, the nonneutral plasma is assumed to consist of three components: electrons in the cathode region (j=b), positively charged ions (j=i), and plasma electrons (j=e). The macroscopic cold-fluid model used in the equilibrium (Sec. II) and stability (Secs. III-VI) analysis is based on the continuity and momentum transfer equations for the density $n_j(\underset{\sim}{x},t)$ and mean velocity $\underset{\sim}{V}_j(\underset{\sim}{x},t)$. Moreover, the electric field $\underset{\sim}{E}(\underset{\sim}{x},t)=-\nabla\phi(\underset{\sim}{x},t)$ is determined self-consistently from Poisson's equation, and $\partial/\partial z=0$ is assumed for both equilibrium and perturbed quantities.

Under steady-state conditions ($\partial/\partial t = 0$), the equilibrium analysis (Sec. II) allows for general density profiles $n_j^0(r)$ (j=b,e,i) and corresponding self-consistent radial electric field [Eq. (5)]

$$E_r^0 = \sum_j 4\pi e_j \frac{1}{r}\int_a^r dr'r'\,n_j^0(r') .$$

Moreover, equilibrium force balance in the radial direction [Eqs. (8) and (11)] can be used to determine the angular rotation velocity $\omega_{rj}(r) = V_{\theta j}^0(r)/r$ of the j'th component fluid element. For slow rotational equilibria satisfying $\omega_{rj}^{-}(r=a)=0$, the rotation velocities are given by [Eqs. (13) and (14)]

$$\omega_{rj}^{-}(r) = \frac{1}{2}\left\{\omega_{ce} - [\omega_{ce}^{2} - 4\omega_{ce}\omega_{E}(r)]^{1/2}\right\}, \quad j=b,e,$$

$$\omega_{rj}^{-}(r) = \frac{1}{2}\left\{-\omega_{ci} + [\omega_{ci}^{2} + 4\omega_{ci}\omega_{E}(r)]^{1/2}\right\}, \quad j=i,$$

in the regions where $n_j^0(r)$ is non-zero. Here, $\omega_E(r) = -cE_r^0/rB_0$ is the $\underset{\sim}{E}^0 \times B_0\hat{\underset{\sim}{e}}_z$ rotation frequency, $\omega_{ce} = eB_0/m_ec$ and $\omega_{ci} = Z_ieB_0/m_ic$ are the cyclotron frequencies, and Z_i is the degree of ionization of the ions. As specific examples, detailed equilibrium properties are investigated for two cases: a neutral plasma in the anode region (Sec. II.B and Fig. 2), and ion-contaminated cathode electrons (Sec. II.C and Fig. 4).

Stability properties are investigated in Sec. III for small-amplitude electrostatic perturbations about general equilibrium profiles $n_j^0(r)$, $E_r^0(r)$ and $\omega_{rj}^{-}(r)$. Expressing $\delta\phi(r,\theta,t) = \sum_{\ell}\delta\phi^{\ell}(r)\exp(i\ell\theta-i\omega t)$, where $\mathrm{Im}\omega > 0$ corresponds to instability, the linearized cold-fluid-Poisson equations give the eigenvalue equation for $\delta\phi^{\ell}(r)$ [Eq. (42)] [20]

$$\frac{1}{r}\frac{\partial}{\partial r}\left[r\left(1+\sum_j \chi_j\right)\frac{\partial}{\partial r}\delta\phi^{\ell}\right] - \frac{\ell^2}{r^2}\left(1+\sum_j\chi_j\right)\delta\phi^{\ell}$$

$$= -\frac{\ell\delta\phi^{\ell}}{r}\sum_j \frac{1}{\omega-\ell\omega_{rj}^{-}}\frac{\partial}{\partial r}\left[\frac{\omega_{pj}^2(\varepsilon_j\omega_{cj} + \omega_{rj}^{-})}{\nu_j^2}\right]$$

where $\omega_{pj}^2(r) = 4\pi n_j^0(r)e_j^2/m_j$, $\varepsilon_j = \mathrm{sgn}\,e_j$, the effective susceptibility $\chi_j(r,\omega)$ is defined by [Eq. (43)]

$$\chi_j(r,\omega) = -\frac{\omega_{pj}^2(r)}{\nu_j^2(r,\omega)},$$

and $\nu_j^2(r,\omega)$ is defined by [Eq. (47)]

$$\nu_j^2(r,\omega) = (\omega-\ell\bar{\omega}_{rj})^2 - \left[\omega_{cj}^2 + 2\epsilon_j\omega_{cj}\omega_E(r) - \frac{4\pi e_j}{m_j}\sum_k e_k n_k^0(r)\right].$$

The summations $\sum_j$ and $\sum_k$ are overall plasma components (b,e,i), and Eq. (42) is to be solved subject to the boundary conditions $\delta\phi^\ell(r=a) = 0 = \delta\phi^\ell(r=b)$. The exact eigenvalue equation (42) is simplified in Sec. III.B for the special case of rectangular density profiles for the cathode electrons and for the neutral plasma ions and electrons in the anode region (Fig. 2). The resulting eigenvalue equation (48), together with the definitions in Eqs. (19) - (21) and Eqs. (49) - (54), have a wide range of applicability and are analyzed numerically in Sec. VI. That is, in Eqs. (48) - (54), there is no a priori assumption that the diode aspect ratio is large, that the density is low, etc.

As an example that is analytically tractable, in Sec. IV (see also Fig. 5) we simplify the eigenvalue equation (48) in circumstances where the anode plasma density is low [Eq. (55)], the cathode electrons are strongly magnetized [Eq. (56)], the diode aspect ratio is large [Eq. (57)], the perturbation frequency is low [Eq. (58)], and the anode plasma is in contact with the cathode electrons [Eq. (59)]. This gives the approximate eigenvalue equation [Eq. (66)]

$$\frac{1}{r}\frac{\partial}{\partial r}\left[r\left(1+\chi_i\right)\frac{\partial}{\partial r}\delta\phi^\ell\right] - \frac{\ell^2}{r^2}\left(1+\chi_i\right)\delta\phi^\ell$$

$$= \frac{\ell\delta\phi^\ell}{r}\;\frac{(\hat{\omega}_{pb}^2/\omega_{ce})}{\omega-\ell\omega_E(r)}\;\delta(r-r_b),$$

where $\chi_i(r,\omega)$ is defined by [Eq. (64)]

$$\chi_i(r,\omega) = \begin{cases} 0 \ , & a < r < r_b \\ -\dfrac{\hat{\omega}_{pi}^2}{(\omega - \ell\hat{\omega}_{ri}^-)^2 - (\omega_{ci}^2 + 2\omega_{ci}\hat{\Omega}_E)} \ , & r_b < r < b \ . \end{cases}$$

Here, $\hat{\Omega}_E = \omega_E(r_b) = (\hat{\omega}_{pb}^2/\omega_{ce})(r_b - a)/r_b$ [Eqs. (60) and (62)], $\hat{\omega}_{pi}^2 = 4\pi\hat{n}_i Z_i^2 e^2/m_i$, $\hat{\omega}_{pb}^2 = 4\pi\hat{n}_b e^2/m_e$, and $\hat{\omega}_{ri}^- = (1/2)\{-\omega_{ci} + [\omega_{ci}^2 + 4\omega_{ci}\hat{\Omega}_E]^{1/2}\}$ [Eq. (61)]. It is clear from Eq. (66) that the surface-charge perturbation on the cathode electron layer can couple to the dielectric response of the plasma ions in the anode region. Solving Eq. (66) for a large-aspect-ratio diode with (b-a)/a<<1 gives the approximate dispersion relation [Eq. (75)]

$$\left(1 + \frac{\Delta_p}{\Delta_b}\right) - \frac{\hat{\omega}_{pi}^2}{(\omega - \ell\hat{\omega}_{ri}^-)^2 - (\omega_{ci}^2 + 2\omega_{ci}\hat{\Omega}_E)} = -\frac{\Delta_p}{\Delta_b}\,\frac{\ell\hat{\Omega}_E}{\omega - \ell\hat{\Omega}_E}$$

where $\Delta_b = r_b - a$ and $\Delta_p = b - r_b$ (Fig. 5), and Δ_b, $\Delta_p << r_b$ is assumed. The dispersion relation (75) is analyzed in Sec. IV and stability properties are investigated over a wide range of the dimensionless parameters $\omega_{ci}/\hat{\Omega}_E = (Z_i m_e/m_i)(\omega_{ce}^2/\hat{\omega}_{pb}^2)(r_b/\Delta_b)$ and $\hat{\omega}_{pi}^2/\hat{\Omega}_E^2 = (Z_i\hat{n}_i/\hat{n}_b)(r_b/\Delta_b)(\omega_{ci}/\hat{\Omega}_E)$. A strong variant of the ion resonance instability[12] is found for a wide range of system parameters.

Although the assumptions in Sec. IV are somewhat restrictive, the analysis clearly establishes the existence and qualitative features of the ion resonance instability and the fact that the plasma ions in the anode region can strongly couple to the cathode electrons.

As a second example that is analytically tractable, in Sec. V we investigate the eigenvalue equation (48) in circumstances where the anode plasma is not in contact with the cathode electrons [Fig. 2 and Eq. (81)]. Assuming high-frequency perturbations [Eq. (83)], unmagnetized ions [Eqs. (82) and (84)], and low-density electrons [Eq. (85)], it is found that the cathode electrons and anode plasma electrons combine to give the diocotron instability driven by electron velocity shear over the interval a<r<b. For infinitely massive ions, the resulting approximate eigenvalue equation (86) is solved exactly to give the dispersion relation [Eq. (93)]

$$\left[1 - \left(\frac{b}{r_p}\right)^{2\ell}\right]\left[1 + \frac{[1-(a/r_b)^{2\ell}]}{\omega/\omega_D - \ell(r_b^2-a^2)/r_b^2}\right]$$

$$= \left[1 + \frac{(\hat{n}_e/\hat{n}_b)[1-(b/r_p)^{2\ell}]}{\omega/\omega_D - \ell(r_b^2-a^2)/r_p^2}\right]\left[1 - \left(\frac{a}{r_p}\right)^{2\ell}\right.$$

$$\left. + \left(1 - \frac{r_b^{\;2\ell}}{r_p^{\;2\ell}}\right)\frac{[1-(a/r_b)^{2\ell}]}{\omega/\omega_D - \ell(r_b^2-a^2)/r_b^2}\right] ,$$

which determines the complex oscillation frequency ω in terms of geometric factors, the density ratio $\hat{n}_e/\hat{n}_b$, and the diocotron frequency $\omega_D=\hat{\omega}_{pb}^2/2\omega_{ce}$. In Sec. V, the dispersion relation (93) is used to investigate detailed stability properties over a wide range of system parameters $\hat{n}_e/\hat{n}_b$, r_p/a, r_b/a, and harominc number ℓ. In the unstable region of parameter space, it is found that the instability growth rate can be substantial (in the range of 0.1 ω_D), even within the context of the low-density assumption made in Sec. V [Eq. (85)].

Finally, in Sec. VI, we make use of the exact eigenvalue equation (48) to investigate numerically electrostatic stability properties for the choice of rectangular density profiles illustrated in Fig. 2. The anode plasma is assumed to be electrically neutral hydrogen plasma ($\hat{n}_e=\hat{n}_i$). No a priori assumption is made that the cathode electron density (as measured by $s_b=\hat{\omega}_{pb}^2/\omega_{ce}^2$) or the anode plasma density (as measured by $s_e=\hat{\omega}_{pe}^2/\omega_{ce}^2$) is small. In the absence of anode plasma ($s_e=0$), the conventional diocotron instability[1] driven by the cathode electrons is recovered. At low cathode electron density this instability is extremely weak ($\mathrm{Im}\omega/\omega_{ce}<10^{-4}$ for $s_b=0.1$ and $s_e=0$), although the growth rate does become substantial as s_b is increased to larger values. In the presence of anode plasma ($s_e\neq 0$), the numerical analysis in Sec. VI shows that both the anode plasma ions and the anode plasma electrons can have a large influence on stability behavior, even at low density. Indeed, the presence of the anode plasma introduces a new low-frequency mode (ion resonance instability) in which there is a strong coupling between the cathode electrons and the anode plasma ions. Moreover, the conventional high-frequency stability properties calculated for $s_e=0$ are significantly modified by the coupling between the cathode electrons and the anode plasma electrons. For example, for the parameters chosen in Fig. 12(b), it is found that $\mathrm{Im}\omega/\omega_{ce}=3.5\times10^{-4}$ for $s_e=0$ and $s_b=0.2$, whereas $\mathrm{Im}\omega/\omega_{ce}=10^{-2}$ for $s_e=0.1$ and $s_b=0.2$. In Sec. VI, the numerical studies of detailed stability properties are carried out for a wide range of system parameters s_b, s_e, diode aspect ratio, etc.

II. COLD-FLUID EQUILIBRIUM FOR A CYLINDRICAL DIODE

A. Equilibrium Model and Assumptions

We consider here the steady-state equilibrium properties ($\partial/\partial t = 0$) of a cold, nonneutral plasma[11] confined in the cylindrical diode configuration illustrated in Fig. 1. The nonneutral plasma is generally assumed to consist of three components: cathode electrons ($j = b$), positively charged ions ($j = i$), and plasma electrons ($j = e$). The plasma electrons may overlap spatially with the ions, e.g., for the case of a neutral plasma in the vicinity of the anode (Fig. 2). As illustrated in Fig. 1, the cathode is located at $r = a$ and the anode at $r = b$, where $d = b - a$ is the anode-cathode spacing. Moreover, the nonneutral plasma is immersed in a uniform applied magnetic field

$$\underset{\sim}{B}_0 = B_0 \hat{\underset{\sim}{e}}_z . \tag{1}$$

For simplicity, the present analysis is based on a nonrelativistic, electrostatic, cold-fluid model for each plasma component ($j = b,e,i$). In equilibrium ($\partial/\partial t = 0$), the following simplifying assumptions are also made:

(a) All equilibrium properties are uniform in the z-direction ($\partial/\partial z = 0$), and there is no equilibrium electric field parallel to $B_0\hat{\underset{\sim}{e}}_z$, i.e., $\underset{\sim}{E}^0(\underset{\sim}{x})\cdot\hat{\underset{\sim}{e}}_z = 0$. All equilibrium properties are assumed to be azimuthally symmetric ($\partial/\partial\theta = 0$) about the diode axis, e.g., the equilibrium density and azimuthal flow velocity components satisfy

$$n_j^0(\underset{\sim}{x}) = n_j^0(r) \ ,$$

$$\underset{\sim}{V}_j^0(\underset{\sim}{x}) = V_{\theta j}^0(r)\underset{\sim}{\hat{e}}_\theta \ , \tag{2}$$

where $\underset{\sim}{\hat{e}}_\theta$ is a unit vector in the θ-direction, and $r=(x^2+y^2)^{1/2}$ is the radial distance from the axis of symmetry.

(b) Equilibrium diamagnetic effects are assumed to be negligibly small in comparison with the applied magnetic field $B_0\underset{\sim}{\hat{e}}_z$. That is, the equilibrium azimuthal current $\sum_j n_j^0(r)e_jV_{\theta j}^0(r)$ generally produces an axial self-magnetic field $B_z^s(r)$. The present analysis assumes that $|B_z^s(r)|<<B_0$.

(c) In general, the plasma is electrically nonneutral and there is a corresponding equilibrium radial electric field

$$\underset{\sim}{E}_0(\underset{\sim}{x}) = E_r^0(r)\underset{\sim}{\hat{e}}_r \ , \tag{3}$$

where $E_r^0(r)$ is determined self-consistently from the steady-state Poisson equation

$$\frac{1}{r}\frac{\partial}{\partial r}[rE_r^0(r)] = \sum_j 4\pi e_j n_j^0(r) \quad . \tag{4}$$

Here, the summation is over $j = b,e,i$, where $e_j = -e$ for the cathode electrons $(j = b)$ and plasma electrons $(j = e)$. Moreover $e_i = +Z_ie$ for the positive ions, where Z_i is the degree of ionization.

(d) Space-charge limited flow with $E_r^0(r=a) = 0$ is assumed. Integrating Eq. (4) then gives for $E_r^0(r)$

$$E_r^0(r) = \sum_j 4\pi e_j \frac{1}{r}\int_a^r dr'r'n_j^0(r') . \tag{5}$$

Expressing $E_r^0 = -\partial\phi^0/\partial r$, where $\phi^0(r)$ is the equilibrium electrostatic potential, we impose the boundary conditions

$$\begin{aligned} \phi_0(r=a) &= 0 \ , \\ \phi_0(r=b) &= V_s \ , \end{aligned} \tag{6}$$

where the anode voltage V_s consistent with Eq. (5) and $E_r^0(r=a) = 0$ is given by

$$V_s = \phi_0(b) = -\sum_j 4\pi e_j \int_a^r \frac{dr''}{r''} \int_a^{r''} dr' r' n_j^0(r') . \tag{7}$$

(e) Finally, within the context of the present nonrelativistic, cold-fluid model, equilibrium radial force balance on the j'th component fluid element can be expressed as

$$-\frac{m_j V_{\theta j}^{0\,2}(r)}{r} = e_j \left[E_r^0(r) + \frac{1}{c} V_{\theta j}^0(r) B_0 \right] , \tag{8}$$

corresponding to a balance of centrifugal, electric and magnetic forces in the region where $n_j^0(r)$ is non-zero.

In the subsequent analysis, it is convenient to introduce the equilibrium angular rotation velocity $\omega_{rj}(r)$ defined by

$$V_{\theta j}^0(r) = \omega_{rj}(r) r , \tag{9}$$

and the $\underset{\sim}{E}^0 \times B_0 \hat{\underset{\sim}{e}}_z$ rotation frequency $\omega_E(r)$ defined by

$$\omega_E(r) = -\frac{cE_r^0(r)}{rB_0} = -\sum_j \frac{4\pi e_j c}{B_0 r^2} \int_a^r dr' r' n_j^0(r') . \tag{10}$$

Making use of Eqs. (9) and (10), the equilibrium force balance equation (8) can be expressed as

$$\omega_{rj}^{2}(r) + \varepsilon_j\omega_{cj}\omega_{rj}(r) - \varepsilon_j\omega_{cj}\omega_E(r) = 0, \tag{11}$$

where

$$\omega_{cj} = \frac{|e_j|B_0}{m_j c}\ , \quad \varepsilon_j = \mathrm{sgn}\,e_j . \tag{12}$$

Equation (11) generally supports two solutions for ω_{rj}, corresponding to fast (ω_{rj}^{+}) and slow (ω_{rj}^{-}) rotational equilibria. For present purposes, we consider slow rotational equilibria satisfying $\omega_{rj}^{-}(r = a) = 0$. Therefore, in the regions where $n_j^0(r)$ is non-zero, Eq. (11) gives

$$\omega_{rj} \equiv \omega_{rj}^{-}(r) = \frac{1}{2}\left\{ \omega_{ce} - [\omega_{ce}^{2} - 4\omega_{ce}\omega_E(r)]^{1/2}\right\},\ j = b,e \tag{13}$$

for the cathode and plasma electrons, and

$$\omega_{ri} \equiv \omega_{ri}^{-}(r) = \frac{1}{2}\left\{ -\omega_{ci} + [\omega_{ci}^{2} + 4\omega_{ci}\omega_E(r)]^{1/2} \right\},\ j = i, \tag{14}$$

for the plasma ions. Here, $\omega_E(r)$ is defined in Eq. (10), and $\omega_{ce} = eB_0/m_e c$ and $\omega_{ci} = Z_i eB_0/m_i c$ are the cyclotron frequencies.

B. Neutral Anode Plasma

As a first equilibrium example, we consider the case illustrated in Fig. 2. The cathode electrons $(j = b)$ are assumed to have the rectangular density profile

$$n_b^0(r) = \begin{cases} \hat{n}_b = \text{const.},\ a < r < r_b, \\ \\ 0\ ,\ r_b < r < b\ . \end{cases} \tag{15}$$

Moreover, there is a neutral plasma in the vicinity of the anode with ion density profile

$$n_i^0(r) = \begin{cases} 0, \ a < r < r_p \ , \\ \hat{n}_i = \text{const.}, \ r_p < r < b \ . \end{cases} \tag{16}$$

The electrons are assumed to provide complete charge neutralization in the region $r_p < r < b$ with

$$n_e^0(r) = Z_i n_i^0(r) . \tag{17}$$

Making use of Eqs. (15) - (17), Poisson's equation (4) can be integrated to give

$$E_r^0 = \begin{cases} \dfrac{-2\pi\hat{n}_b e}{r}\,(r^2 - a^2), & a < r < r_b, \\[2ex] \dfrac{-2\pi\hat{n}_b e}{r}\,(r_b{}^2 - a^2), & r_b < r < b. \end{cases} \tag{18}$$

Defining $\hat{\omega}_{pb}^2 = 4\pi\hat{n}_b e^2/m_e$, and making use of $\omega_E(r) = -cE_r^0/rB_0$, Eqs. (13) and (18) give for the electrons in the cathode region

$$\omega_{rb}^-(r) = \frac{1}{2}\left\{ \omega_{ce} - \left[\omega_{ce}^2 - 2\hat{\omega}_{pb}^2 \left(\frac{r^2 - a^2}{r^2}\right)\right]^{1/2} \right\}, \ a<r<r_b \ . \tag{19}$$

On the other hand, from Eqs. (13) and (18), the plasma electrons in the anode region have equilibrium rotation velocity

$$\omega_{re}^{-}(r) = \frac{1}{2}\left\{\omega_{ce} - \left[\omega_{ce}^2 - 2\hat{\omega}_{pb}^2\left(\frac{r_b^2 - a^2}{r^2}\right)\right]^{1/2}\right\}, \quad r_p<r<b, \tag{20}$$

and from Eqs. (14) and (18), $\omega_{ri}^{-}(r)$ is given by

$$\omega_{ri}^{-}(r) = \frac{1}{2}\left\{ -\omega_{ci} + \left[\omega_{ci}^2 + 2\frac{Z_i m_e}{m_i}\hat{\omega}_{pb}^2\left(\frac{r_b^2-a^2}{r^2}\right)\right]^{1/2}\right\}, \quad r_p<r<b \tag{21}$$

for the plasma ions in the anode region. The rotation velocities $\omega_{rj}(r)\,(j=b,e,i)$ are illustrated schematically in Fig. 2.

It is convenient to introduce (for $a<r<r_b$)

$$\omega_E(r) = \frac{\hat{\omega}_{pb}^2}{2\omega_{ce}}\left(\frac{r^2-a^2}{r^2}\right) \tag{22}$$

in Eq. (19). For

$$\frac{2\hat{\omega}_{pb}^2}{\omega_{ce}^2}\left(\frac{r_b^2-a^2}{r_b^2}\right) << 1, \tag{23}$$

it is clear from Eq. (19) that ω_{rb}^{-} can be approximated by

$$\omega_{rb}^{-}(r) = \omega_E(r), \quad a<r<r_b, \tag{24}$$

where $\omega_E(r)$ is defined in Eq. (22). For a large-aspect-ratio diode with $(r_b^2 - a^2)/r_b^2 << 1$, note that Eq. (23) is easily satisfied even at moderately high electron densities with $2\hat{\omega}_{pb}^2 \lesssim \omega_{ce}^2$. Making use of Eq. (23), the angular velocity of the plasma electrons is given by the approximate expression

$$\omega_{re}^{-}(r) = \hat{\Omega}_E \frac{r_b^2}{r^2}, \quad r_p<r<b, \tag{25}$$

where

$$\hat{\Omega}_E \equiv \omega_E(r_b) = \frac{\hat{\omega}_{pb}^2}{2\omega_{ce}} \left(\frac{r_b^2 - a^2}{r_b^2} \right) . \qquad (26)$$

Moreover, Eq. (21) can be expressed as

$$\omega_{ri}^-(r) = \frac{1}{2} \left\{ -\omega_{ci} + \left[\omega_{ci}^2 + 4\omega_{ci}\hat{\Omega}_E \frac{r_b^2}{r^2} \right]^{1/2} \right\}, \ r_p < r < b. \qquad (27)$$

For strongly magnetized ions with $\hat{\Omega}_E << \omega_{ci}/4$, Eq. (27) reduces to the $\underset{\sim}{E}^0 \times \underset{\sim}{B}_0$ rotation frequency

$$\omega_{ri}^-(r) = \hat{\Omega}_E \frac{r_b^2}{r^2} , \ r_p < r < b. \qquad (28)$$

On the other hand, for weakly magnetized ions with $\hat{\Omega}_E >> \omega_{ci}/4$, Eq. (27) reduces to

$$\omega_{ri}^-(r) = (\omega_{ci}\hat{\Omega}_E)^{1/2} \frac{r_b}{r} , \ r_p < r < b. \qquad (29)$$

In both cases, for a diode with moderately large aspect ratio, $(b-a)^2/a^2 << 1$, Eqs. (27) - (29) exhibit only a weak variation of $\omega_{ri}^-(r)$ with r over the anode plasma region ($r_p < r < b$).

Figure 3 shows a plot of ω_{ri}^- versus $\hat{\Omega}_E/\omega_{ci}$ for the case $r_p = r_b$ and $r = r_b$. Note from Eq. (26) that $\hat{\Omega}_E/\omega_{ci}$ is related to other equilibrium parameters by

$$\frac{\hat{\Omega}_E}{\omega_{ci}} = \frac{m_i}{Z_i m_e} \frac{\hat{\omega}_{pb}^2}{2\omega_{ce}^2} \left(\frac{r_b^2 - a^2}{r_b^2} \right) . \qquad (30)$$

Therefore, the region $\hat{\Omega}_E/\omega_{ci} >> 1$ in Fig. 3 corresponds to sufficiently high density of the cathode electrons that the inequality

$$\frac{\hat{\omega}_{pb}^2}{2\omega_{ce}^2}\left(\frac{r_b^2 - a^2}{r_b^2}\right) >> \frac{Z_i m_e}{m_i} \tag{31}$$

is satisfied.

C. Ion-Contaminated Cathode Electrons

As a second equilibrium example, we consider the case illustrated in Fig. 4 where the cathode electrons are partially neutralized by a positive ion background.[12] In particular, it is assumed that $n_b^0(r)$ has the rectangular profile

$$n_b^0(r) = \begin{cases} \hat{n}_b = \text{const.} \ , & a < r < r_b , \\ 0 & , \ r_b < r < b , \end{cases} \tag{32}$$

and that the ion density profile $n_i^0(r)$ is related to $n_b^0(r)$ by

$$Z_i n_i^0(r) = f\, n_b^0(r) , \tag{33}$$

where $f = \text{const.}$ is the fractional charge neutralization. There is not a second component of electrons in the present equilibrium example, i.e., $n_e^0(r) = 0$. Making use of Eqs. (32) and (33), we determine $E_r^0(r)$ from Eq. (5). This gives

$$E_r^0 = \begin{cases} \dfrac{-2\pi e\hat{n}_b(1-f)}{r}\,(r^2 - a^2) , & a < r < r_b , \\ \dfrac{-2\pi e\hat{n}_b(1-f)}{r}\,(r_b^2 - a^2) , & r_b < r < b . \end{cases} \tag{34}$$

Therefore, from Eq. (10), $\omega_E(r)$ is given by

$$\omega_E(r) = \frac{\hat{\omega}_{pb}^2}{2\omega_{ce}} (1-f) \frac{(r^2-a^2)}{r^2} \qquad (35)$$

over the interval $a<r<r_b$. For $\omega_E(r) \ll \omega_{ce}/4$, it follows from Eq. (13) that the angular rotation velocity of the cathode electrons can be approximated by

$$\omega_{rb}^-(r) = \omega_E(r), \quad a < r < r_b, \qquad (36)$$

where $\omega_E(r)$ is defined in Eq. (35). Finally, defining $\hat{\Omega}_E \equiv \omega_E(r_b) = (\hat{\omega}_{pb}^2/2\omega_{ce})(1-f)(r_b^2-a^2)/r_b^2$, and making use of Eqs. (14) and (35), the ion rotation velocity can be expressed as

$$\omega_{ri}^-(r) = \frac{1}{2}\left\{ -\omega_{ci} + \left[\omega_{ci}^2 + 4\omega_{ci}\hat{\Omega}_E \frac{r_b^2}{r^2} \frac{(r^2-a^2)}{(r_b^2-a^2)} \right]^{1/2} \right\}, a<r<r_b. \qquad (37)$$

The rotation velocities in Eqs. (36) and (37) are illustrated schematically in Fig. 4. In contrast to Eq. (27), where the ions in the anode region satisfy $\omega_{ri}^-(r) \simeq$ const., we note from Eq. (37) that $\omega_{ri}^-(r)$ generally has a strong dependence on r for the case where the cathode electrons are partially charge neutralized by the background ions.

III. ELECTROSTATIC EIGENVALUE EQUATION

A. General Eigenvalue Equation

We now investigate stability properties for electrostatic perturbations about the general class of cold-fluid equilibrium profiles described in Sec. II.A. The stability analysis is based on the nonrelativistic cold-fluid equations of continuity and momentum transfer together with Poisson's equation for the perturbed electric field $\delta \underset{\sim}{E}(\underset{\sim}{x},t) = -\nabla\delta\phi(\underset{\sim}{x},t)$. Flute perturbations with $\partial/\partial z = 0$ are assumed, and all perturbed quantities are expressed as

$$\delta\psi(r,\theta,t) = \sum_{\ell=-\infty}^{\infty} \delta\psi^{\ell}(r)\exp(i\ell\theta - i\omega t) ,$$

where ℓ is the azimuthal harmonic number, and ω is the complex eigenfrequency, with $\mathrm{Im}\omega>0$ corresponding to instability. For electrostatic perturbations about a cylindrically symmetric equilibrium characterized by density profiles $n_j^0(r)$ $(j=b,e,i)$, radial electric field $E_r^0(r)$ [Eq. (5)], and equilibrium rotation velocity $\omega_{rj}^{-}(r)$ [Eqs. (11), (13) and (14)], the linearized continuity and cold-fluid momentum transfer equations are given by[20]

$$-i(\omega-\ell\omega_{rj}^{-})\delta n_j^{\ell} + \frac{1}{r}\frac{\partial}{\partial r}(r n_j^0 \delta V_{jr}^{\ell}) + \frac{i\ell}{r} n_j^0 \delta V_{j\theta}^{\ell} = 0, \qquad (38)$$

$$-i(\omega-\ell\omega_{rj}^{-})\delta V_{jr}^{\ell} - (\epsilon_j\omega_{cj} + 2\omega_{rj}^{-})\delta V_{j\theta}^{\ell} = -\frac{e_j}{m_j}\frac{\partial}{\partial r}\delta\phi^{\ell}, \qquad (39)$$

$$-i(\omega-\ell\omega_{rj}^{-})\delta V_{j\theta}^{\ell} + \left[\epsilon_j\omega_{cj} + \frac{1}{r}\frac{\partial}{\partial r}(r^2\omega_{rj}^{-})\right]\delta V_{jr}^{\ell} = -\frac{e_j}{m_j}\frac{i\ell\delta\phi^{\ell}}{r} . \qquad (40)$$

Here, $\delta n_j^\ell(r)$, $\delta V_{jr}^\ell(r)$ and $\delta V_{j\theta}^\ell(r)$ are the Fourier amplitudes for the perturbed density, radial flow velocity, and azimuthal flow velocity, respectively, and the notation is otherwise identical to Sec. II.A. Moreover, the perturbed potential amplitude $\delta\phi^\ell(r)$ is determined self-consistently in terms of $\delta n_j^\ell(r)$ from Poisson's equation

$$\frac{1}{r}\frac{\partial}{\partial r}\left(r\frac{\partial}{\partial r}\,\delta\phi^\ell\right)-\frac{\ell^2}{r^2}\,\delta\phi^\ell = -\sum_j 4\pi e_j\delta n_j^\ell \ , \tag{41}$$

where the summation $\sum_j$ is over all plasma components j=b,e,i.

After some straightforward algebra that utilizes Eqs. (38) - (40) to express δn_j^ℓ in terms of $\delta\phi^\ell$, Poisson's equation (41) can be expressed as[20]

$$\begin{aligned}\frac{1}{r}\frac{\partial}{\partial r}\left[r\left(1+\sum_j\chi_j\right)\frac{\partial}{\partial r}\,\delta\phi^\ell\right]-\frac{\ell^2}{r^2}\left(1+\sum_j\chi_j\right)\delta\phi^\ell \\ = \frac{-\ell\delta\phi^\ell}{r}\sum_j\frac{1}{\omega-\ell\omega_{rj}^{-}}\,\frac{\partial}{\partial r}\left[\frac{\omega_{pj}^2(\varepsilon_j\omega_{cj}+2\omega_{rj}^{-})}{\nu_j^2}\right] ,\end{aligned}\tag{42}$$

where $\omega_{pj}^2(r) = 4\pi n_j^0(r)e_j^2/m_j$, and the effective susceptibility $\chi_j(r,\omega)$ for component j is defined by

$$\chi_j(r,\omega) = -\frac{\omega_{pj}^2(r)}{\nu_j^2(r,\omega)} \ , \tag{43}$$

where

$$\nu_j^2(r,\omega) = (\omega-\ell\omega_{rj}^{-})^2-(\varepsilon_j\omega_{cj}+2\omega_{rj}^{-})\left[\varepsilon_j\omega_{cj}+\frac{1}{r}\frac{\partial}{\partial r}(r^2\omega_{rj}^{-})\right] . \tag{44}$$

For general equilibrium profiles $n_j^0(r)$, the rotation velocities $\omega_{rj}^{-}(r)$ occurring in Eqs. (42) and (44) are determined self-consistently from Eqs. (13) and (14) for plasma components $j=b,e,i$. The eigenvalue equation (42) for $\delta\phi^{\ell}$ must of course be solved subject to the boundary conditions

$$\delta\phi^{\ell}(r=a) = 0 = \delta\phi^{\ell}(r=b) \tag{45}$$

at the cathode $(r=a)$ and anode $(r=b)$. Making use of the equilibrium force balance equation (11) and Poisson's equation (4), the expression for $\nu_j^2(r,\omega)$ in Eq. (44) can be further simplified. In particular, it can be shown that

$$\begin{aligned}&\left(\varepsilon_j\omega_{cj} + 2\omega_{rj}^{-}\right)\left[\varepsilon_j\omega_{cj} + \frac{1}{r}\frac{\partial}{\partial r}\left(r^2\omega_{rj}^{-}\right)\right]\\ &\qquad = \omega_{cj}^2 + 2\varepsilon_j\omega_{cj}\omega_E(r) - \frac{4\pi e_j}{m_j}\sum_k e_k n_k^0(r),\end{aligned} \tag{46}$$

where $\omega_E(r)$ is defined in Eq. (10), and the summation $\sum_k$ extends over all plasma components $k=b,e,i$. Substituting Eq. (46) into Eq. (44) then gives

$$\nu_j^2(r,\omega) = (\omega - \ell\omega_{rj}^{-})^2 - \left[\omega_{cj}^2 + 2\varepsilon_j\omega_{cj}\omega_E(r) - \frac{4\pi e_j}{m_j}\sum_k e_k n_k^0(r)\right]. \tag{47}$$

To summarize, Eq. (42) is the electrostatic eigenvalue equation that determines the eigenfunction $\delta\phi^{\ell}(r)$ and the complex eigenfrequency ω for general equilibrium density profiles $n_j^0(r)$, $j=b,e,i$. The quantities $\chi_j(r,\omega)$ and $\nu_j^2(r,\omega)$ are defined in Eqs. (43) and (44), and $\omega_E(r)$ and $\omega_{rj}^{-}(r)$ are determined self-consistently from Eqs. (10), (13) and (14).

B. Eigenvalue Equation for Rectangular Density Profiles

We now simplify the eigenvalue equation (42) for the perturbations about the equilibrium discussed in Sec. II.B and illustrated in Fig. 2. The density profiles are assumed to be rectangular [Eqs. (15) - (17)] and there is a neutral plasma in the vicinity of the anode. The eigenvalue equation (42) can be expressed as

$$\frac{1}{r}\frac{\partial}{\partial r}\left[r\left(1+\sum_j \chi_j\right)\frac{\partial}{\partial r}\delta\phi^\ell\right] - \frac{\ell^2}{r^2}\left(1+\sum_j\chi_j\right)\delta\phi^\ell$$

$$= \frac{\ell\delta\phi^\ell}{r}\sum_j \frac{1}{\omega-\ell\bar{\omega}_{rj}}\frac{\partial}{\partial r}\left[\chi_j\left(\epsilon_j\omega_{cj}+2\bar{\omega}_{rj}\right)\right] \quad , \tag{48}$$

where $\chi_j(r,\omega)$ is defined in Eq. (43).

For the electrons in the cathode region (j=b), referring to Sec. II.B and Fig. 2, the effective susceptibility is

$$\chi_b(r,\omega) = \begin{cases} -\dfrac{\hat{\omega}_{pb}^2}{\nu_b^2} \ , & a < r < r_b \ , \\ \\ 0 \ , & r_b < r < b \ , \end{cases} \tag{49}$$

where ν_b^2 is defined by [Eq. (47)]

$$\nu_b^2(r,\omega) = (\omega-\ell\bar{\omega}_{rb})^2 - \left[\omega_{ce}^2 - \hat{\omega}_{pb}^2 - 2\omega_{ce}\omega_E(r)\right]$$

$$= (\omega-\ell\bar{\omega}_{rb})^2 - \left[\omega_{ce}^2 - \hat{\omega}_{pb}^2 - \hat{\omega}_{pb}^2\left(\frac{r^2-a^2}{r^2}\right)\right] \tag{50}$$

for $a < r < r_b$. Here, $\hat{\omega}_{pb}^2 = 4\pi\hat{n}_b e^2/m_e$, and $\omega_{rb}^-(r)$ is defined in Eq. (19).

For the plasma ions in the anode region (j=i), the effective susceptibility $\chi_i(r,\omega)$ is

$$\chi_i(r,\omega) = \begin{cases} 0, & a < r < r_p, \\ -\dfrac{\hat{\omega}_{pi}^2}{\nu_i^2}, & r_p < r < b, \end{cases} \tag{51}$$

where $\hat{\omega}_{pi}^2 = 4\pi\hat{n}_i Z_i^2 e^2/m_i$, and ν_i^2 is defined by [Eq. (47)]

$$\begin{aligned} \nu_i^2(r,\omega) &= (\omega - \ell\omega_{ri}^-)^2 - \left[\omega_{ci}^2 + 2\omega_{ci}\omega_E(r)\right] \\ &= (\omega - \ell\omega_{ri}^-)^2 - \left[\omega_{ci}^2 + \frac{Z_i m_e}{m_i}\hat{\omega}_{pb}^2\left(\frac{r_b^2 - a^2}{r^2}\right)\right] \end{aligned} \tag{52}$$

for $r_p < r < b$. In obtaining Eq. (52) from Eq. (47), we have made use of charge neutrality $[\sum_{j=i,e} n_j^0(r)e_j = 0]$ of the anode plasma [Eq. (17)]. Moreover, $\omega_{ri}^-(r)$ is defined in Eq. (21).

Finally, for the plasma electrons in the anode region (j=e), the effective susceptibility $\chi_e(r,\omega)$ is

$$\chi_e(r,\omega) = \begin{cases} 0, & a < r < r_p, \\ -\dfrac{\hat{\omega}_{pe}^2}{\nu_e^2}, & r_p < r < b, \end{cases} \tag{53}$$

where $\hat{\omega}_{pe}^2 = 4\pi\hat{n}_e e^2/m_e$, and ν_e^2 is defined by [Eq. (47)]

$$\begin{aligned} \nu_e^2(r,\omega) &= (\omega - \ell\omega_{re}^-)^2 - \left[\omega_{ce}^2 - 2\omega_{ce}\omega_E(r)\right] \\ &= (\omega - \ell\omega_{re}^-)^2 - \left[\omega_{ce}^2 - \hat{\omega}_{pb}^2\left(\frac{r_b^2 - a^2}{r^2}\right)\right] \end{aligned} \tag{54}$$

for $r_p < r < b$. Here $\omega_{re}^-(r)$ is defined in Eq. (20) for the plasma electrons in the anode region.

To summarize, the eigenvalue equation (48), together with the definitions in Eqs. (19) - (21) and Eqs. (49) - (54) constitute the final eigenvalue equation for electrostatic perturbations about the equilibrium density profiles specified by Eqs. (15) - (17). In this regard, within the context of the present nonrelativistic, electrostatic, cold-fluid model, the eigenvalue equation (48) is exact. That is, there is no a priori assumption that the diode aspect ratio is large, that the density is low, etc. Therefore, Eqs. (48) - (54) have a wide range of applicability.

The detailed stability properties predicted by Eq. (48) are analyzed numerically in Sec. V for a wide range of equilibrium parameters. In Sec. IV, we investigate Eq. (48) in the low-density, low-frequency regime where the solutions are analytically tractable.

IV. ION RESONANCE INSTABILITY DRIVEN BY ANODE PLASMA IONS

A. Simplified Eigenvalue Equation

As an example that is analytically tractable, we consider the eigenvalue equation (48) for the case of a low-density anode plasma with

$$\hat{n}_i, \hat{n}_e << \hat{n}_b , \qquad (55)$$

and strongly magnetized cathode electrons with

$$\omega_{pb}^2(r) << \omega_{ce}^2 \qquad (56)$$

The equilibrium configuration, effective susceptibilities, etc., correspond to the rectangular profiles considered in Secs. II.B and III.B with the following additional simplifying assumptions:

(a) The cylindrical diode has large aspect ratio with

$$\frac{(b-a)^2}{a^2} << 1. \qquad (57)$$

(b) We examine Eq. (48) for low-frequency perturbations with

$$|\omega - \ell\bar{\omega}_{rb}(r)|^2 << \omega_{ce}^2 . \qquad (58)$$

(c) The anode plasma extends to the edge of the cathode electrons with

$$r_p = r_b \qquad (59)$$

as illustrated in Fig. 5.

Consistent with Eqs. (56) and (57), the angular rotation velocity of the cathode electrons can be approximated by [see also Eqs. (19) and (24)]

$$\begin{aligned}\omega_{rb}^{-}(r) &= \omega_E(r) \\ &= \frac{\hat{\omega}_{pb}^2}{2\omega_{ce}}\left(\frac{r^2 - a^2}{r^2}\right) \simeq \frac{\hat{\omega}_{pb}^2}{\omega_{ce}}\left(\frac{r - a}{r_b}\right)\end{aligned} \tag{60}$$

for $a < r < r_b$. In Eq. (60), we have approximated $(r+a)/r^2 \simeq 2/r_b$ for the case of a large-aspect-ratio diode [Eq. (57)]. Furthermore, from Eqs. (27) and (57), we neglect the (slow) r-variation of $\omega_{ri}^{-}(r)$ and approximate

$$\omega_{ri}^{-}(r) = \hat{\omega}_{ri}^{-} = \frac{1}{2}\left\{-\omega_{ci} + \left[\omega_{ci}^2 + 4\omega_{ci}\hat{\Omega}_E\right]^{1/2}\right\} \tag{61}$$

for $r_b < r < b$, where $\hat{\Omega}_E = \omega_E(r_b)$ is given by

$$\hat{\Omega}_E = \frac{\hat{\omega}_{pb}^2}{\omega_{ce}}\left(\frac{r_b - a}{r_b}\right) . \tag{62}$$

Similarly, the rotation velocity of the electrons in the cathode region [Eqs. (20) and (25)] is approximated by $\omega_{re}^{-}(r) = \hat{\Omega}_E$ for $r_b < r < b$.

We now examine the susceptibility factors occurring on the left-hand side of Eq. (48). Referring to Eqs. (49) and (50), and making use of Eqs. (56), (58) and (60), we find $\nu_b^2 \simeq \omega_{ce}^2$. Therefore, χ_b can be approximated by

$$\chi_b(r,\omega) = \begin{cases} \dfrac{\hat{\omega}_{pb}^2}{\omega_{ce}^2}, & a < r < r_b, \\ \\ 0, & r_b < r < b. \end{cases} \tag{63}$$

Note that $|\chi_b| << 1$ since $\hat{\omega}_{pb}^2 << \omega_{ce}^2$ is assumed. Similarly, from Eqs. (53) and (54), it can be shown for the electrons in the anode region that $\chi_e(r,\omega) \simeq \hat{\omega}_{pe}^2/\omega_{ce}^2$ over the range $r_b < r < b$. Moreover, $|\chi_e| << 1$ by virtue of Eqs. (55) and (56). Finally, from Eqs. (51), (52), (61) and (62), the ion susceptibility $\chi_i(r,\omega)$ can be expressed as

$$\chi_i(r,\omega) = \begin{cases} 0, & a < r < r_b, \\ \\ -\dfrac{\hat{\omega}_{pi}^2}{(\omega - \ell\hat{\bar{\omega}}_{ri})^2 - (\omega_{ci}^2 + 2\omega_{ci}\hat{\Omega}_E)}, & r_b<r<b, \end{cases} \tag{64}$$

where $\hat{\bar{\omega}}_{ri}$ and $\hat{\Omega}_E$ are defined in Eqs. (61) and (62).

With regard to the right-hand side of the eigenvalue equation (48), we retain the perturbed surface-charge contribution from the cathode electrons, which is proportional to $\partial\omega_{pb}^2(r)/\partial r = -\hat{\omega}_{pb}^2\delta(r - r_b)$. However, we neglect the perturbed surface-charge contributions from the anode plasma electrons and ions ($j = e,i$) by virtue of the low-density assumption in Eq. (55). Approximating

$$\frac{\omega_{pb}^2(r)}{\nu_b^2(r,\omega)}(-\omega_{ce} + 2\bar{\omega}_{rb}) = \frac{\omega_{pb}^2(r)}{\omega_{ce}} \tag{65}$$

on the right-hand side of Eq. (48), and $|\chi_b| << 1$ and $|\chi_e| << 1$ on the left-hand side of Eq. (48), the eigenvalue equation can be expressed as

$$\frac{1}{r}\frac{\partial}{\partial r}\left\{ r\left[1+\chi_i(r,\omega)\right]\frac{\partial}{\partial r}\,\delta\phi^{\ell}\right\} - \frac{\ell^2}{r^2}\left[1+\chi_i(r,\omega)\right]\delta\phi^{\ell}$$

$$= \frac{\ell\delta\phi^{\ell}}{r}\,\frac{(\hat{\omega}_{pb}^2/\omega_{ce})}{\omega-\ell\omega_E(r)}\,\delta(r-r_b)\,, \tag{66}$$

where $\chi_i(r,\omega)$ is defined in Eq. (64).

To summarize, Eq. (66) is an excellent approximation to the exact eigenvalue equation (48) in circumstances where the anode plasma density is low [Eq. (55)], the cathode electrons are strongly magnetized [Eq. (56)], the diode aspect ratio is large [Eq. (57)], and the perturbation frequency is low [Eq. (58)]. It is clear from Eq. (66), that the surface-charge perturbation on the cathode electrons can couple to the dielectric response of the plasma ions in the anode region.

B. Dispersion Relation and Analytic Results

In this section, we solve the approximate eigenvalue equation (66) subject to the boundary conditions $\delta\phi^{\ell}(r=a) = 0 = \delta\phi^{\ell}(r=b)$. Referring to Fig. 5, in Region I ($a < r < r_b$), Eq. (66) reduces to $(1/r)(\partial/\partial r)(r\partial\delta\phi^{\ell}/\partial r) - (\ell^2/r^2)\delta\phi^{\ell} = 0$, which has the solution

$$\delta\phi_{I}^{\ell}(r) = A\left[\left(\frac{r}{a}\right)^{\ell} - \left(\frac{a}{r}\right)^{\ell}\right] \times \left[\left(\frac{r_b}{a}\right)^{\ell} - \left(\frac{a}{r_b}\right)^{\ell}\right]^{-1}, \quad a < r < r_b. \tag{67}$$

Moreover, in Region II ($r_b < r < b$), Eq. (66) again reduces to $(1/r)(\partial/\partial r)(r\partial\delta\phi^{\ell}/\partial r) - (\ell^2/r^2)\delta\phi^{\ell} = 0$. The solution for $\delta\phi^{\ell}(r)$ in Region II that is continuous with Eq. (67) at $r = r_b$ and vanishes at $r = b$ is given by

$$\delta\phi_{II}^{\ell}(r) = A\left[\left(\frac{r}{b}\right)^{\ell} - \left(\frac{b}{r}\right)^{\ell}\right] \times \left[\left(\frac{r_b}{b}\right)^{\ell} - \left(\frac{b}{r_b}\right)^{\ell}\right]^{-1}, \quad r_b < r < b. \tag{68}$$

The remaining boundary condition is obtained by integrating Eq. (66) across the surface at $r = r_b$ (Fig. 5). Multiplying Eq. (66) by r and integrating from $r_b(1 - \delta)$ to $r_b(1 + \delta)$ with $\delta \to 0_+$ gives

$$r_b\left[1 - \frac{\hat{\omega}_{pi}^2}{(\omega - \ell\hat{\bar{\omega}}_{ri})^2 - (\omega_{ci}^2 + 2\omega_{ci}\hat{\Omega}_E)}\right]\left[\frac{\partial}{\partial r}\,\delta\phi_{II}^{\ell}\right]_{r=r_b} - r_b\left[\frac{\partial}{\partial r}\,\delta\phi_{I}^{\ell}\right]_{r=r_b} = \frac{\ell\delta\phi_{I}^{\ell}(r_b)}{\omega - \ell\omega_E(r_b)}\,\frac{\hat{\omega}_{pb}^2}{\omega_{ce}}. \tag{69}$$

Equation (69) relates the discontinuity in $(\partial\delta\phi^{\ell}/\partial r)$ at $r = r_b$ to the perturbed surface-charge density.

We define

$$\begin{aligned} r_b - a &= \Delta_b \ , \\ b - r_b &= \Delta_p \ , \end{aligned} \tag{70}$$

where Δ_b is the width of the cathode electron region and Δ_p is the width of the anode plasma region (Fig. 5). Moreover, from Eqs. (60) and (70),

$$\omega_E(r_b) = \hat{\Omega}_E = \frac{\hat{\omega}_{pb}^2}{\omega_{ce}} \frac{\Delta_b}{r_b} \ . \tag{71}$$

Substituting Eqs. (67) and (68) into Eq. (69) then gives

$$\begin{aligned} &- \ell \left[1 - \frac{\hat{\omega}_{pi}^2}{(\omega - \ell\hat{\omega}_{ri})^2 - (\omega_{ci}^2 + 2\omega_{ci}\hat{\Omega}_E)} \right] \frac{1 + (r_b/b)^{2\ell}}{1 - (r_b/b)^{2\ell}} \\ &\qquad - \ell \ \frac{1 + (a/r_b)^{2\ell}}{1 - (a/r_b)^{2\ell}} = \frac{r_b}{\Delta_b} \frac{\ell\hat{\Omega}_E}{\omega - \ell\hat{\Omega}_E} \ . \end{aligned} \tag{72}$$

Equation (72) plays the role of a dispersion relation that determines the complex eigenfrequency ω in terms of other system parameters.

For a large-aspect-ratio diode, we Taylor expand $[1 + (r_b/b)^{2\ell}]/[1 - (r_b/b)^{2\ell}] \simeq b/\ell\Delta_p$ and $[1+(a/r_b)^{2\ell}]/[1 - (a/r_b)^{2\ell}] \simeq a/\ell\Delta_b$, where

$$\frac{\ell\Delta_p}{b} \ , \ \frac{\ell\Delta_b}{a} << 1 \tag{73}$$

is assumed. Equation (72) then reduces to

$$1 + \frac{\Delta_p}{\Delta_b}\frac{r_b}{b} - \frac{\hat{\omega}_{pi}^2}{(\omega - \ell\hat{\omega}_{ri}^-)^2 - (\omega_{ci}^2 + 2\omega_{ci}\hat{\Omega}_E)}$$

$$= -\frac{r_b}{b}\frac{\Delta_p}{\Delta_b}\frac{\ell\hat{\Omega}_E}{\omega - \ell\hat{\Omega}_E} \; . \tag{74}$$

Taking $r_b/b \simeq 1$ in Eq. (74) for a large-aspect-ratio diode gives the approximate dispersion relation

$$\left(1 + \frac{\Delta_p}{\Delta_b}\right) - \frac{\hat{\omega}_{pi}^2}{(\omega - \ell\hat{\omega}_{ri}^-)^2 - (\omega_{ci}^2 + 2\omega_{ci}\hat{\Omega}_E)}$$

$$= -\frac{\Delta_p}{\Delta_b}\frac{\ell\hat{\Omega}_E}{\omega - \ell\hat{\Omega}_E} \; . \tag{75}$$

For the special case of no ions ($\hat{\omega}_{pi}^2 = 0$), Eq. (75) gives the familiar result

$$\omega - \ell\hat{\Omega}_E = -\frac{\Delta_p}{\Delta_b + \Delta_p}\,\ell\hat{\Omega}_E \tag{76}$$

corresponding to stable oscillations on the surface of the electron layer. For $\hat{\omega}_{pi}^2 \neq 0$, however, Eq. (75) can give instability associated with the coupling of these surface oscillations to the plasma ions in the anode region.

Making use of the definitions $\hat{\omega}_{pi}^2 = 4\pi\hat{n}_i Z_i^2 e^2/m_i$ and $\hat{\Omega}_E = (\hat{\omega}_{pb}^2/\omega_{ce})(\Delta_b/r_b)$ [Eq. (62)], two of the dimensionless frequencies occurring in the dispersion relation (75) can be expressed for a large-aspect-ratio diode as

$$\frac{\omega_{ci}}{\hat{\Omega}_E} = \frac{Z_i m_e}{m_i} \frac{\omega_{ce}^2}{\hat{\omega}_{pb}^2} \frac{r_b}{\Delta_b} , \tag{77}$$

$$\begin{aligned} \frac{\hat{\omega}_{pi}^2}{\hat{\Omega}_E^2} &= \frac{Z_i m_e}{m_i} \frac{Z_i \hat{n}_i}{\hat{n}_b} \frac{\omega_{ce}^2}{\hat{\omega}_{pb}^2} \frac{r_b^2}{\Delta_b^2} \\ &= \frac{Z_i \hat{n}_i}{\hat{n}_b} \frac{r_b}{\Delta_b} \frac{\omega_{ci}}{\hat{\Omega}_E} . \end{aligned} \tag{78}$$

Moreover, from Eq. (61), $\hat{\omega}_{ri}^-/\hat{\Omega}_E$ is given by

$$\frac{\hat{\omega}_{ri}^-}{\hat{\Omega}_E} = \frac{1}{2}\left\{ - \frac{\omega_{ci}}{\hat{\Omega}_E} + \left[\frac{\omega_{ci}^2}{\hat{\Omega}_E^2} + 4 \frac{\omega_{ci}}{\hat{\Omega}_E} \right]^{1/2} \right\} . \tag{79}$$

The dispersion relation (75) is a cubic equation for the complex eigenfrequency ω, valid for a large-aspect-ratio diode within the context of the assumptions enumerated at the beginning of Sec. IV.A Making use of Eq. (75), the marginal stability curves ($\mathrm{Im}\omega = 0$) in the parameter space ($\omega_{ci}/\hat{\Omega}_E$, $\hat{\omega}_{pi}^2/\hat{\Omega}_E^2$) are plotted in Fig. 6 for several values of azimuthal harmonic number ℓ and for $\Delta_b/\Delta_p = 3$ [Fig. 6(a)], $\Delta_b/\Delta_p = 1$ [Fig. 6(b)] and $\Delta_b/\Delta_p = 1/3$ [Fig. 6(c)]. For specified ℓ, the regions above the curves in Fig. 6 correspond to instability with $\mathrm{Im}\omega > 0$, whereas the regions below the curves correspond to stable oscillations with $\mathrm{Im}\omega = 0$. Moreover, for the choice of system parameters $\hat{\omega}_{ci}/\hat{\Omega}_E = 0.1$ and $\Delta_b/\Delta_p = 1$, shown in Fig. 7 are plots of normalized growth rate $\mathrm{Im}\omega/\hat{\Omega}_E$ [Fig. 7(a)] and real frequency $\mathrm{Re}\omega/\hat{\Omega}_E$ [Fig. 7(b)] versus $\hat{\omega}_{pi}^2/\hat{\Omega}_E^2$ obtained from Eq. (75). Several features of the stability behavior are noteworthy from Figs. 6 and 7.

(a) First, for weakly magnetized ions with $\omega_{ci}/\hat{\Omega}_E << 1$, it follows from Fig. 6 that instability can exist over a relatively wide range of ion density as measured by $\hat{\omega}_{pi}^2/\hat{\Omega}_E^2$.

(b) Typically, for specified $\omega_{ci}/\hat{\Omega}_E$, Δ_b/Δ_p, and harmonic number ℓ, there is a threshold value of ion density above which instability occurs. For example, for $\omega_{ci}/\hat{\Omega}_E = 0.01$ and a relatively thick cathode electron layer with $\Delta_b/\Delta_p = 3$, it follows from Fig. 6(a) that instability occurs when $\hat{\omega}_{pi}^2/\hat{\Omega}_E^2 > 0.06$ for the $\ell = 1$ mode, and when $\hat{\omega}_{pi}^2/\hat{\Omega}_E^2 > 0.5$ for the $\ell = 2$ mode. On the other hand, for $\omega_{ci}/\hat{\Omega}_E = 0.01$ and $\Delta_b/\Delta_p = 1/3$, which corresponds to a relatively thick anode plasma region and thin cathode electron layer (see Fig. 5), we find from Fig. 6(c) that the threshold for instability occurs at much lower values of $\hat{\omega}_{pi}^2/\hat{\Omega}_E^2$ than the $\Delta_b/\Delta_p = 3$ case analyzed in Fig. 6(a).

(c) From Eq. (75), it can be shown that the minima in the marginal stability curves plotted in Fig. 6 occur for $\hat{\omega}_{pi}^2/\hat{\Omega}_E^2 = 0$ and values of $\omega_{ci}/\hat{\Omega}_E$ determined from

$$\frac{2\Delta_b}{\Delta_b + \Delta_p} = \left[(\eta^2 + 4\eta)^{1/2} - \eta + \frac{2}{\ell}(\eta^2 + 2\eta)^{1/2}\right]_{\eta = \left(\frac{\omega_{ci}}{\hat{\Omega}_E}\right)_M} \tag{80}$$

for $\ell = 1, 2, \ldots$. When $\omega_{ci}/\hat{\Omega}_E$ is less than the value of $(\omega_{ci}/\hat{\Omega}_E)_M$ for $\ell = 1$, it is evident from Figs. 6(a) - 6(c) that the $\ell = 1, 2, \ldots$ modes switch on sequentially as $\hat{\omega}_{pi}^2/\hat{\Omega}_E^2$ is increased. On the other hand, when $\omega_{ci}/\hat{\Omega}_E$ exceeds the value of $(\omega_{ci}/\hat{\Omega}_E)_M$ for $\ell = 1$, it follows from Figs. 6(a) - 6(c) that selected higher mode numbers have a lower threshold value of

$\hat{\omega}_{pi}^2/\hat{\Omega}_E^2$ for instability than the $\ell = 1$ mode. (See also Fig. 7).

(d) As a general remark, for specified $\hat{\omega}_{pi}^2/\hat{\Omega}_E^2$ and mode number ℓ, it is evident from Figs. 6(a) - 6(c) that the range of $\omega_{ci}/\hat{\Omega}_E$ corresponding to instability shifts upward as the thickness of the cathode electron layer is increased relative to the thickness of the anode plasma region. For example, for $\hat{\omega}_{pi}^2/\hat{\Omega}_E^2 = 1$ and $\ell = 7$, it follows from Figs. 6(a) and 6(c) that instability exists for $0.026 < \omega_{ci}/\hat{\Omega}_E < 0.65$ when $\Delta_b/\Delta_p = 1$, and for $0.26 < \omega_{ci}/\hat{\Omega}_E < 1$ when $\Delta_b/\Delta_p = 3$.

(e) In Fig. 7, we plot the normalized growth rate $\text{Im}\omega/\hat{\Omega}_E$ [Fig. 7(a)] and real frequency $\text{Re}\omega/\hat{\Omega}_E$ [Fig. 7(b)] versus $\hat{\omega}_{pi}^2/\hat{\Omega}_E^2$ obtained from Eq. (75) for $\Delta_b/\Delta_p = 1$, $\omega_{ci}/\hat{\Omega}_E = 0.1$, and $\ell = 1,2, \ldots 5$. Referring to Figs. 6(b) and 7(a), we find that as $\hat{\omega}_{pi}^2/\hat{\Omega}_E^2$ is increased, the unstable modes switch on sequentially in the order: $\ell = 2$, $\ell = 3$, $\ell = 1$ and $\ell = 4$, and $\ell = 5$. Moreover, the growth rates for the ion resonance instability inferred from Fig. 7(a) can be substantial. For example, for $\ell = 3$ and $\hat{\omega}_{pi}^2/\hat{\Omega}_E^2 = 0.5$, it follows from Fig. 7(a) that $\text{Im}\omega \simeq 0.5\hat{\Omega}_E = 0.707\ \hat{\omega}_{pi}$. Moreover, for $\ell = 3$ and $\hat{\omega}_{pi}^2/\hat{\Omega}_E^2 = 0.5$, the real oscillation frequency is $\text{Re}\omega \simeq -1.42\hat{\Omega}_E = -2\hat{\omega}_{pi}$ [Fig. 7(b)].

To summarize, in Sec. IV we have investigated analytically properties of the ion resonance instability[12] in circumstances where the anode plasma density is low [Eq. (55)], the cathode electrons are strongly magnetized [Eq. (56)], the diode aspect ratio is large [Eq. (57)], the perturbation frequency is low [Eq. (58)], and the anode plasma is in contact with the cathode electrons [Eq. (59) and Fig. 5]. Although these assumptions are somewhat restrictive, the analysis clearly establishes the existence and qualitative features of the ion resonance instability and the fact that the plasma ions in the anode region can strongly couple to the cathode electrons.

V. DIOCOTRON INSTABILITY DRIVEN BY ANODE PLASMA ELECTRONS

As a second example that is analytically tractable, we consider the eigenvalue equation (48) in circumstances where the anode plasma is not in contact with the cathode electrons, i.e.,

$$r_p > r_b \tag{81}$$

as illustrated in Fig. 2. In this case, the cathode electrons and the anode plasma electrons can combine to give the diocotron instability driven by electron velocity shear over the interval a<r<b. To simplify the analysis and to distinguish this instability from the ion resonance instability discussed in Sec. IV, we make the following additional assumptions:

(a) The maximum rotation frequency of the cathode electrons, $\omega_{rb}^{-}(r_b) = \hat{\Omega}_E$ is much higher than the ion cyclotron frequency, i.e.,

$$\hat{\Omega}_E >> \omega_{ci}. \tag{82}$$

(b) Consistent with Eq. (82), we consider high-frequency perturbations with

$$\omega \underset{\sim}{\approx} \ell\omega_{rb}^{-}(r_b), \tag{83}$$

and treat the anode ions as a tenuous, unmagnetized plasma component satisfying

$$|\omega| >> \omega_{ci}, \ \hat{\omega}_{pi}, \ |\ell\omega_{ri}^{-}(r_p)|. \tag{84}$$

(c) No a priori assumption is made regarding the relative size of the plasma electron density and the cathode electron density $(\hat{n}_e/\hat{n}_b)$. However, for present purposes, it is assumed that

$$\hat{\omega}_{pb}^2,\ \hat{\omega}_{pe}^2 << \omega_{ce}^2, \tag{85}$$

which corresponds to low-density, strongly magnetized electrons.

Making use of Eqs. (82)-(85), it is straightforward to simplify the eigenvalue equation (48) and the related definitions in Eqs. (49)-(54). In particular, the ions are treated as infinitely massive $(m_i\rightarrow\infty)$ and the susceptibilities $\chi_j(r,\omega)(j=b,e,i)$ are approximated by zero on the left-hand side of Eq. (48). Moreover, only the cathode electrons and the anode electrons contribute on the right-hand side of Eq. (48). Making use of Eqs. (82)-(85), the eigenvalue equation (48) can then be approximated by

$$\begin{aligned}&\frac{1}{r}\frac{\partial}{\partial r} r \frac{\partial}{\partial r}\delta\phi^{\ell} - \frac{\ell^2}{r^2}\delta\phi^{\ell}\\ &\qquad = \frac{\ell\delta\phi^{\ell}}{r}\frac{\hat{\omega}_{pb}^2}{\omega_{ce}}\left[\frac{\delta(r-r_b)}{\omega-\ell\hat{\Omega}_E} - \frac{\hat{n}_e}{\hat{n}_b}\frac{\delta(r-r_p)}{\omega-\ell\hat{\Omega}_E r_b^2/r_p^2}\right].\end{aligned} \tag{86}$$

Here, $\hat{\omega}_{pb}^2 = 4\pi\hat{n}_b e^2/m_e$, and $\hat{\Omega}_E = \omega_{rb}^-(r_b) = \omega_E(r_b)$ is defined by [Eqs. (22) and (24)]

$$\hat{\Omega}_E = \omega_D\left(\frac{r_b^2 - a^2}{r_b^2}\right), \tag{87}$$

where

$$\omega_D = \frac{\hat{\omega}_{pb}^2}{2\omega_{ce}} \tag{88}$$

is the effective diocotron frequency in the absence of an internal conductor $(a = 0)$. It is clear from Eq. (86) that the two source terms on the right-hand side correspond to surface-charge perturbations at the surface of the cathode electron layer $(r = r_b)$ and the anode electrons $(r = r_p)$. Also note in Eq. (86) that no a priori assumption has been made that the diode aspect ratio is large. That is, Eq. (86) is valid for arbitrary $b/a > 1$.

Referring to Fig. 2, the eigenvalue equation (86) reduces to the vacuum eigenvalue equation $r^{-1}(\partial/\partial r)(r\partial\delta\phi^{\ell}/\partial r) - (\ell^2/r^2)\delta\phi^{\ell} = 0$ within the cathode electron layer $(a \leq r < r_b)$, in the vacuum region $(r_b < r < r_p)$, and within the anode plasma $(r_p < r \leq b)$. Therefore, the solution to Eq. (86) that satisfies $\delta\phi^{\ell}(r=a) = 0 = \delta\phi^{\ell}(r=b)$ is given trivially by

$$\delta\phi^{\ell}(r) = \begin{cases} A\left[\left(\frac{r}{a}\right)^{\ell} - \left(\frac{a}{r}\right)^{\ell}\right], & a \leq r < r_b, \\ Br^{\ell} + C/r^{\ell}, & r_b < r < r_p, \\ D\left[\left(\frac{r}{b}\right)^{\ell} - \left(\frac{b}{r}\right)^{\ell}\right], & r_p < r \leq b. \end{cases} \tag{89}$$

Two of the boundary conditions required in Eq. (89) are continuity of $\delta\phi^{\ell}(r)$ at $r = r_b$ and at $r = r_p$, i.e.,

$$\begin{aligned} \lim_{\varepsilon \to 0_+} \delta\phi^{\ell}(r_b - \varepsilon) &= \lim_{\varepsilon \to 0_+} \delta\phi^{\ell}(r_b + \varepsilon), \\ \lim_{\varepsilon \to 0_+} \delta\phi^{\ell}(r_p - \varepsilon) &= \lim_{\varepsilon \to 0_+} \delta\phi^{\ell}(r_p - \varepsilon). \end{aligned} \tag{90}$$

The two remaining boundary conditions are obtained by multiplying Eq. (86) by r and integrating across the discontinuities at $r = r_b$ and at $r = r_p$. This readily gives

$$\lim_{\varepsilon\to 0_+} \left\{ \left[r \frac{\partial}{\partial r} \delta\phi^{\ell} \right]_{r_b+\varepsilon} - \left[r \frac{\partial}{\partial r} \delta\phi^{\ell} \right]_{r_b-\varepsilon} \right\} = 2\ell\delta\phi^{\ell}(r_b) \frac{\omega_D}{\omega - \ell\hat{\Omega}_E} , \tag{91}$$

and

$$\lim_{\varepsilon\to 0_+} \left\{ \left[r \frac{\partial}{\partial r} \delta\phi^{\ell} \right]_{r_p+\varepsilon} - \left[r \frac{\partial}{\partial r} \delta\phi^{\ell} \right]_{r_p-\varepsilon} \right\} = -2\ell\delta\phi^{\ell}(r_p) \frac{\hat{n}_e}{\hat{n}_b} \frac{\omega_D}{\omega - \ell\hat{\Omega}_E r_b^2/r_p^2} . \tag{92}$$

Substituting Eq. (89) into Eqs. (90)-(92), after some straightforward algebra we obtain the dispersion relation

$$\begin{aligned} &\left[1 - \left(\frac{b}{r_p}\right)^{2\ell}\right] \left[1 + \frac{[1 - (a/r_b)^{2\ell}]}{\omega/\omega_D - \ell(r_b^2 - a^2)/r_b^2}\right] \\ &= \left[1 + \frac{(\hat{n}_e/\hat{n}_b)[1 - (b/r_p)^{2\ell}]}{\omega/\omega_D - \ell(r_b^2 - a^2)/r_p^2}\right] \left[1 - \left(\frac{a}{r_p}\right)^{2\ell} \right. \\ &\left. + \left(1 - \frac{r_b^{2\ell}}{r_p^{2\ell}}\right) \frac{[1 - (a/r_b)^{2\ell}]}{\omega/\omega_D - \ell(r_b^2 - a^2)/r_b^2}\right] . \end{aligned} \tag{93}$$

Equation (93) can be used to determine the complex oscillation frequency ω over a wide range of system parameters $\hat{n}_e/\hat{n}_b$, r_b/a, r_p/a and b/a. For the special case where the anode electrons are in contact with the cathode electrons ($r_p = r_b$), Eq. (93) supports only stable oscillations with $\mathrm{Im}\omega = 0$. This is expected since for $r_p = r_b$ the electron density profile is monotonic over the entire interval $a<r<b$ (Fig. 2).[21]

For $r_p > r_b$, the linear dispersion relation in Eq. (93) has been solved numerically for the complex eigenfrequency ω. Typical numerical results are summarized in Fig. 8 where (a) the normalized growth rate $\mathrm{Im}\omega/\omega_D$ and (b) the real oscillation frequency $\mathrm{Re}\omega/\omega_D$ obtained from Eq. (93) are plotted versus r_p/a for the choice of parameters $b/a = 2$, $r_b/a = 1.5$, density ratio $\hat{n}_e/\hat{n}_b = 0.1$, and several values of the azimuthal mode number ℓ. Several points are noteworthy from Fig. 8. First, the maximum growth rate can be a substantial fraction of the diocotron frequency ω_D, thereby indicating a strong instability. Second, for each value of ℓ, the range of r_p/a corresponding to instability ($\mathrm{Im}\omega > 0$) is relatively narrow. Evidently, from Fig. 8(a), high mode numbers ℓ are excited when the anode plasma boundary (r_p/a) approaches the boundary of the cathode electrons ($r_b/a = 1.5$). In the limit, however, instability ceases ($\mathrm{Im}\omega = 0$) when $r_p = r_b$. Finally, from Fig. 8(b), for specified value of harmonic number ℓ, the real frequency of the unstable mode is almost independent of r_p/a.

Shown in Fig. 9 are plots of (a) the marginal stability boundaries in the parameter space (r_p/a, ℓ), and (b) the maximum growth rate and the corresponding real oscillation frequency obtained from Eq. (93) for $\hat{n}_e/\hat{n}_b = 0.2$ and parameters otherwise identical to Fig. 8. The cross-hatched region in Fig. 9(a) corresponds to instability ($\mathrm{Im}\omega > 0$). The dashed curve in Fig. 9(a) represents the conditions for maximum growth rate. For the choice of parameters in Fig. 9, only mode numbers satisfying $\ell \geq 4$ exhibit instability. As shown in Fig. 9(b), the real oscillation frequency is linearly proportional to ℓ, although the maximum growth rate saturates quickly with increasing ℓ.

In order to illustrate the dependence of stability behavior on the density ratio $\hat{n}_e/\hat{n}_b$, in Fig. 10 are plotted (a) the marginal stability boundaries in the parameter space $(r_p/a, \hat{n}_e/\hat{n}_b)$, and (b) the maximum growth rate and the corresponding real oscillation frequency obtained from Eq. (93) for $\ell = 5$ and parameters otherwise identical to Fig. 8. From Fig. 10(b), for this choice of system parameters, we note that the maximum growth rate occurs for density ratio $\hat{n}_e/\hat{n}_b \simeq 0.4$. That is, the instability growth rate does not continue to increase for $\hat{n}_e/\hat{n}_b \gtrsim 0.4$.

Finally, the dependence of stability properties on the location of the boundary of the cathode electrons (r_b/a) is illustrated in Fig. 11, where (a) the marginal stability boundaries in the parameter space $(r_p/a, r_b/a)$, and (b) the maximum growth rate and corresponding real oscillation frequency are presented for $\hat{n}_e/\hat{n}_b = 0.2$ and parameters otherwise identical to Fig. 10. The dashed curve in Fig. 11(a) corresponds to maximum growth rate. Evidently, from Fig. 11(b), for $b/a = 2$ and $\hat{n}_e/\hat{n}_b = 0.2$, the strongest instability occurs for $r_b/a \simeq 1.5$.

VI. NUMERICAL RESULTS

In this section, we make use of the exact eigenvalue equation (48) and the related definitions in Eqs. (49)-(54) and Eqs. (19)-(21) to investigate numerically the stability properties for electrostatic perturbations about the equilibrium density profiles illustrated in Fig. 2. No a priori assumption is made that the anode plasma density or cathode electron density is low or that the electrons are strongly magnetized. In solving Eq. (48), we impose the boundary conditions $\delta\phi^{\ell}(r=a)=0=\delta\phi^{\ell}(r=b)$, and the anode plasma between $r=r_p$ and $r=b$ is assumed to be hyrdogen plasma with

$$Z_i = 1 \text{ and } \frac{m_e}{m_i} = \frac{1}{1836} \; . \tag{94}$$

Typical numerical results are illustrated in Figs. 12 and 13 for the choice of geometric factors

$$\frac{r_b}{a} = 1.2, \; \frac{r_p}{a} = 1.4 \text{ and } \frac{b}{a} = 1.6, \tag{95}$$

corresponding to a moderate aspect ratio diode. The stability results in Fig. 12 correspond to the high-frequency (electron-driven) branch (Sec. V), whereas Fig. 13 illustrates stability behavior for the low-frequency branch (ion resonance instability)[12] in which the anode plasma ions couple strongly to the cathode electrons (Sec. IV).

Beginning with the high-frequency branch, the normalized real frequency $\mathrm{Re}\omega/\omega_{ce}$ and the growth rate $\mathrm{Im}\omega/\omega_{ce}$ obtained from Eq. (48)

are plotted in Fig. 12 versus normalized cathode electron density $s_b=\hat{\omega}_{pb}^2/\omega_{ce}^2$ for values of $s_e=\hat{\omega}_{pe}^2/\omega_{ce}^2$ ranging from $s_e=0$ (no anode plasma) to $s_e=0.5$ (dense anode plasma). The numerical plots are presented for azimuthal mode numbers $\ell=4$ [Fig. 12(a)], $\ell=8$ [Fig 12(b)] and $\ell=12$ [Fig. 12(c)].

For no anode plasma ($s_e=0$) and low-density cathode electrons ($s_b=\hat{\omega}_{pb}^2/\omega_{ce}^2<<1$), it is clear from Fig. 12 that the instability growth rate is extremely small ($\mathrm{Im}\omega/\omega_{ce}<10^{-4}$ for $s_b<0.1$). Moreover, for $s_b<<1$ and $s_e=0$, the real oscillation frequency in Fig. 12 connects smoothly onto the analytic result [see Eq. (93) with $\hat{n}_e=0$]

$$\frac{\mathrm{Re}\omega}{\omega_{ce}} = \frac{\hat{\omega}_{pb}^2}{2\omega_{ce}}\left\{\ell\left(1-\frac{a^2}{r_b^2}\right)-\frac{[1-(r_b/b)^{2\ell}]}{[1-(a/b)^{2\ell}]}\,[1-(a/r_b)^{2\ell}]\right\}. \qquad (96)$$

As the cathode electron density (s_b) is increased for $s_e=0$, it is clear from Fig. 12 that the growth rate and real frequency increase monotonically, at least for values of $\hat{\omega}_{pb}^2/\omega_{ce}^2$ up to 0.7. In addition, $\mathrm{Re}\omega$ and $\mathrm{Im}\omega$ increase with mode number ℓ for the range of ℓ presented in Fig. 12. The $s_e=0$ results in Fig. 12 are consistent with earlier numerical studies of electrostatic stability properties carried out for rectangular cathode electron density profile in Ref. 1.

For non-zero anode plasma density ($s_e\neq0$), it is clear from Fig. 12 that the instability growth rate and real oscillation frequency are enhanced relative to the $s_e=0$ case. This is due to a coupling between the plasma electrons and the cathode electrons. Evidently, this coupling can be particularly strong in the low-density regime (Sec. V). For example, for $\ell=8$ and $s_b=\hat{\omega}_{pb}^2/\omega_{ce}^2=0.2$ it follows from Fig. 12(b) that $\mathrm{Im}\omega/\omega_{ce}=3.5\times10^{-4}$ for $s_e=\omega_{pe}^2/\omega_{ce}^2=0$, whereas $\mathrm{Im}\omega/\omega_{ce}=1\times10^{-2}$ for $s_e=\hat{\omega}_{pe}^2/\omega_{ce}^2=0.1$. This corresponds to a thirty-fold increase in the growth rate produced by the strong interaction of the anode electrons with the cathode electrons. As s_b and s_e are increased further, the growth rate is still enhanced relative to the $s_e=0$ case, but not by the same large factors as in the low-density regime. For the parameters chosen in Figs. 12(a)-12(c), we also note that the enhancement in growth rate as s_e is increased is more pronounced at larger ℓ-values, whereas the enhancement in real oscillation frequency as s_e is increased tends to be weaker at larger ℓ-values.

We now consider Fig. 13 where the numerical results obtained from Eq. (48) are presented for both the low-frequency (ion-driven) branch as well as the high-frequency (electron-driven) branch. In Fig. 13, and throughout the remainder of this paper (Figs. 14 and 15), the high-frequency and low-frequency solutions are labeled by the numbers 1 and 2, respectively. Shown in Fig. 13 are plots of the normalized real frequency $\mathrm{Re}\omega/\omega_{ce}$ and growth rate $\mathrm{Im}\omega/\omega_{ce}$ for the mode number $\ell=8$ and geometric parameters specified by $r_b/a=1.2$, $r_p/a=1.4$ and $b/a=1.6$ [Eq. (95)]. In Fig. 13(a), the real frequency and growth rate are plotted versus $s_b=\hat{\omega}_{pb}^2/\omega_{ce}^2$ for fixed density ratio $\hat{n}_e/\hat{n}_b=0.5$. On the other hand, in Fig. 13(b), the real frequency and growth rate are plotted versus density ratio $\hat{n}_e/\hat{n}_b$ for a fixed value of $\hat{\omega}_{pb}^2/\omega_{ce}^2=0.4$. Several features of the stability behavior are evident from Fig. 13. First, the real oscillation frequency for the ion-driven branch (curve set #2) is about an order-of-magnitude lower (or somewhat less) than the real oscillation frequency for the high-frequency branch (curve set #1), at least for the range of parameters analyzed in Fig. 13. Second, for fixed density ratio $\hat{n}_e/\hat{n}_b=0.5$ and increasing values of $\hat{\omega}_{pb}^2/\omega_{ce}^2$, it is clear from Fig. 13(a) that the growth rate for the ion resonance instability increases monotonically (albeit slowly), whereas the growth rate for the high-frequency branch exhibits a secondary maximum for $s_b \simeq 0.25$ (see also Fig. 12). On the other hand, for fixed value of $\hat{\omega}_{pb}^2/\omega_{ce}^2=0.4$ and increasing density ratio $\hat{n}_e/\hat{n}_b$, we find from Fig. 13(b) that the growth rate for the ion resonance instability increases rapidly and begins to level off at $\mathrm{Im}\omega \simeq 0.0045\omega_{ce}$ for $\hat{n}_e/\hat{n}_b \gtrsim 0.3$, whereas the growth rate for the high-frequency branch increases slowly over the entire interval $0<\hat{n}_e/\hat{n}_b<0.5$. Another important feature evident from Fig. 13 is that the growth rate of the ion resonance instability can be substantial. Indeed, the growth rates of the two branches are comparable over most of the parameter range analyzed in Fig. 13(b). This is a very important result, since the ions participate as an active component for the low-frequency branch (curve set #2), and would be expected to exhibit a strong nonlinear response to the instability.

A region of strong ion resonance instability is also illustrated in Fig. 14 where the normalized real frequency $\mathrm{Re}\omega/\omega_{ce}$ and growth rate $\mathrm{Im}\omega/\omega_{ce}$ are plotted versus $s_b=\hat{\omega}_{pb}^2/\omega_{ce}^2$ for mode number $\ell=8$, fixed density ratio $\hat{n}_e/\hat{n}_b=0.5$, and diode aspect ratio increased from a/(b-a)=1.67 (in Figs. 12 and 13) to a/(b-a)= 4.76 (in Fig. 14). For the parameter range analyzed in Fig. 14, the real frequency of the two branches differ by less than a factor of two. On the other hand, the growth rate of the ion resonance instability (curve set #2) is substantially larger than the growth rate of the high-frequency branch (curve set #1) over a wide range of cathode electron density ($s_b \lesssim 0.4$).

The strong dependence of instability growth rate and real oscillation frequency on diode aspect ratio was evident from the analytic studies of the two branches presented in Secs. IV and V. This is further illustrated in Fig. 15, where the normalized real frequency $\mathrm{Re}\omega/\omega_{ce}$ and growth rate $\mathrm{Im}\omega/\omega_{ce}$ obtained from Eq. (48) are plotted versus normalized diode thickness Δ defined by

$$\Delta = \frac{b-a}{a} \tag{97}$$

As in Figs. 12-14, the relative thickness of the cathode electron layer, the vacuum region, and the anode plasma, each correspond to one-third of the total cathode-anode spacing. That is, in Fig. 15,

$$\frac{r_b}{a} = 1 + \frac{1}{3}\Delta, \ \frac{r_p}{a} = 1 + \frac{2}{3}\Delta. \tag{98}$$

Moreover, $\ell=8$ and fixed density ratio $\hat{n}_e/\hat{n}_b=0.5$ are assumed in Fig. 15, with $s_b=\hat{\omega}_{pb}^2/\omega_{ce}^2=0.4$ in Fig. 15(a) and $s_b=0.7$ in Fig. 15(b). Comparing Figs. 15(a) and 15(b), it is found that the plots of the real oscillation frequency for both branches and the growth rate for the ion resonance instability (curve set #2) are relatively insensitive to increasing the cathode electron density from $s_b = \hat{\omega}_{pb}^2/\omega_{ce}^2 = 0.4$ [Fig. 15(a)] to $\hat{\omega}_{pb}^2/\omega_{ce}^2 = 0.7$ [Fig. 15(b)]. On the other hand, there is a significant increase in the growth rate of the high-frequency branch (curve set #1) as s_b is increased. In addition, for the parameter range analyzed in Fig. 15, there is an abrupt increase in the growth rate of the ion resonance instability as Δ is increased, with $\mathrm{Im}\omega$ beginning to level off at $\mathrm{Im}\omega \simeq 0.005\omega_{ce}$ for $\Delta \gtrsim 0.5$. Moreover, it is evident from Fig. 15 that the growth rate of the high-frequency branch exhibits a secondary maximum (for $\Delta \simeq 0.1$) as Δ is increased. Although the detailed physical reason for this growth enhancement (secondary maximum) is not understood at the present time, the reader will recall from the analytic studies in Sec. V that the instability growth rate of the high-frequency branch exhibits a very sensitive dependence on the geometric factors r_b/a, r_p/a and b/a.

VII. CONCLUSIONS

In this paper, we have made use of the macroscopic cold-fluid-Poisson equations to investigate collective instabilities driven by anode plasma ions and electrons in a nonrelativistic cylindrical diode with applied magnetic field $B_0\hat{e}_z$. Following a review of equilibrium properties (Sec. II), the electrostatic eigenvalue equation is derived (Sec. III) and investigated analytically (Secs. IV and V) and numerically (Sec. VI) assuming flute perturbations with $\partial/\partial z=0$. Particular emphasis is placed on the influence of the anode plasma on stability behavior assuming uniform cathode electron density ($\hat{n}_b$) extending from $r=a$ to $r=r_b$, and uniform anode plasma density ($\hat{n}_e=Z_i\hat{n}_i$) extending from $r=r_p$ to $r=b$. Depending on the cathode electron density (as measured by $s_b=\hat{\omega}_{pb}^2/\omega_{ce}^2$), the anode plasma density (as measured by $s_e=\hat{\omega}_{pe}^2/\omega_{ce}^2$), the diode aspect ratio, etc., it is found that there can be a strong coupling of the anode plasma to the cathode electrons, and a concomitant large influence on detailed stability behavior. In particular, the presence of the anode plasma ions introduces a new low-frequency mode (ion resonance instability) in which there is a strong coupling of the anode plasma ions to the cathode electrons (Secs. IV and VI). Moreover, the conventional high-frequency stability properties calculated for $s_e=0$ are significantly modified by the coupling between the cathode electrons and the anode plasma electrons (Secs. V and VI). For example, for $b/a=1.6$, $r_b/a=1.2$, $r_p/a=1.4$, $\ell=8$ and $s_b=0.2$, it is found that

$\mathrm{Im}\omega/\omega_{ce}=3.5\times 10^{-4}$ for $s_e=0$, whereas $\mathrm{Im}\omega/\omega_{ce}=10^{-2}$ for $s_e=0.1$, corresponding to a thirty-fold increase in instability growth rate [Fig. 12(b)].

ACKNOWLEDGMENTS

This research was supported by Sandia National Laboratories and in part by the Office of Naval Research.

REFERENCES

1. R.C. Davidson and K. Tsang, Phys. Rev. A29, 488 (1984).
2. R.C. Davidson, K. Tsang and J. Swegle, Phys. Fluids 27, 2332 (1984).
3. J. Swegle, Phys. Fluids 26, 1670 (1983).
4. J. Swegle and E. Ott, Phys. Fluids 24, 1821 (1981).
5. J. Swegle and E. Ott, Phys. Rev. Lett. 46, 929 (1981).
6. R.C. Davidson, Phys. Fluids 24, in press (1984).
7. J.P. VanDevender, J.P. Quintenz, R.J. Leeper, D.J. Johnson and J.T. Crow, J. Appl. Phys. 52, 4 (1981).
8. R.H. Levy, Phys. Fluids 8, 1288 (1965).
9. R.J. Briggs, J.D. Daugherty and R.H. Levy, Phys. Fluids 13, 421 (1970).
10. O. Buneman, R.H. Levy and L.M. Linson, J. Appl. Phys. 37, 3203 (1966).
11. R.C. Davidson, Theory of Nonneutral Plasmas (Benjamin, Reading, Mass., 1974).
12. R.H. Levy, J.D. Daugherty and O. Buneman, Phys. Fluids 12, 2616 (1969).
13. I. Haber and A.W. Maschke, Phys. Rev. Lett. 42, 1479 (1979).
14. R.C. Davidson, Ref. 11, pp. 62-66.
15. D.G. Koshkarev and P.R. Zenkevich, Particle Accelerators 3, 1 (1972).
16. R.C. Davidson and H.S. Uhm, Phys. Fluids 21, 265 (1978).
17. R.C. Davidson and H.S. Uhm, Plasma Physics 10, 579 (1978).
18. H.S. Uhm and R.C. Davidson, Particle Accelerators 11, 135 (1980).
19. H.S. Uhm and R.C. Davidson, Phys. Fluids 25, 2334 (1982).
20. R.C. Davidson, Ref. 11, pp. 41-45.
21. R.C. Davidson, Phys. Fluids 27, 1804 (1984).

FIGURE CAPTIONS

Fig. 1 Cylindrical diode configuration with cathode located at r=a and anode at r=b. Equilibrium flow is in the θ-direction, and the equilibrium space-charge density $\sum_j n_j^0(r)e_j$ produces a radial electric field $E_r^0(r)$ [Eq. (5)].

Fig. 2 Plots of equilibrium density $n_j^0(r)$ and angular velocity $\omega_{rj}^-(r)$ versus r obtained from Eqs. (15) - (17) and Eqs. (19) - (21). Electrons in the cathode region have a rectangular density profile extending from r=a to $r=r_b$. The plasma in the anode region is electrically neutral with $Z_i n_i^0(r) = n_e^0(r)$, and extends from $r=r_p$ to r=b.

Fig. 3 Plot of $\omega_{ri}^-(r_b)$ versus $\hat{\Omega}_E/\omega_{ci} = (m_i/Z_i m_e)(\hat{\omega}_{pb}^2/2\omega_{ce}^2) \times [(r_b^2-a^2)/r_b^2]$ obtained from Eq. (27) for $r_p=r_b$ and $r=r_b$.

Fig. 4 Plots of equilibrium density $n_j^0(r)$ and angular velocity $\omega_{rj}^-(r)$ versus r obtained from Eqs. (32) and (33) and Eqs. (36) and (37). The cathode electrons are partially charge neutralized by positive ions with $Z_i n_i^0(r) = f\, n_b^0(r)$, where f=const.=fractional charge neutralization.

Fig. 5 Model density profiles used for electrostatic stability analysis in Sec. IV. The anode plasma density is low with $\hat{n}_i$, $\hat{n}_e << \hat{n}_b$ [Eq. (55)], and the anode plasma extends to the edge of the cathode electrons with $r_p=r_b$ [Eq. (59)].

Fig. 6. Plots of marginal stability curves in the parameter space $(\omega_{ci}/\hat{\Omega}_E,\ \hat{\omega}_{pi}^2/\hat{\Omega}_E^2)$ obtained from Eq. (75) for several values of harmonic number ℓ and (a) $\Delta_b/\Delta_p = 3$, (b) $\Delta_b/\Delta_p = 1$, and (c) $\Delta_b/\Delta_p = 1/3$. Regions above the curves are unstable ($\mathrm{Im}\omega > 0$), and regions below the curves correspond to stable oscillations ($\mathrm{Im}\omega = 0$).

Fig. 7. Plots of (a) normalized growth rate $\mathrm{Im}\omega/\hat{\Omega}_E$ and (b) normalized real oscillation frequency $(\mathrm{Re}\omega - \ell\hat{\Omega}_E)/\hat{\Omega}_E$ versus $\hat{\omega}_{pi}^2/\hat{\Omega}_E^2$ obtained from Eq. (75) for $\Delta_b/\Delta_p = 1$, $\omega_{ci}/\hat{\Omega}_E = 0.1$, and several values of harmonic number ℓ.

Fig. 8. Plots of (a) the normalized growth rate $\mathrm{Im}\omega/\omega_D$, and (b) real oscillation frequency $\mathrm{Re}\omega/\omega_D$ versus r_p/a obtained from Eq. (93) for $b/a = 2$, $r_b/a = 1.5$, $\hat{n}_e/\hat{n}_b = 0.1$ and several values of harmonic number ℓ.

Fig. 9. Plots of (a) the marginal stability boundaries in the parameter space $(r_p/a,\ \ell)$, and (b) the maximum growth rate and corresponding real oscillation frequency obtained from Eq. (93) for $\hat{n}_e/\hat{n}_b = 0.2$ and parameters otherwise identical to Fig. 8. The dashed curve in Fig. 9(a) corresponds to maximum growth rate.

Fig. 10. Plots of (a) the marginal stability boundaries in the parameter space $(r_p/a,\ \hat{n}_e/\hat{n}_b)$, and (b) the maximum growth rate and corresponding real oscillation frequency obtained from Eq. (93) for $\ell = 5$ and

parameters otherwise identical to Fig. 8. The dashed curve in Fig. 10(a) corresponds to maximum growth rate.

Fig. 11 Plots of (a) the marginal stability boundaries in the parameter space $(r_p/a,\ r_b/a)$, and (b) the maximum growth rate and corresponding real oscillation frequency obtained from Eq. (93) for $\hat{n}_e/\hat{n}_b=0.2$ and parameters otherwise identical to Fig. 10. The dashed curve in Fig. 11(a) corresponds to maximum growth rate.

Fig. 12 Plots of normalized real frequence $\mathrm{Re}\omega/\omega_{ce}$ and growth rate $\mathrm{Im}\omega/\omega_{ce}$ versus $\hat{\omega}_{pb}^2/\omega_{ce}^2$ obtained from Eq. (48) for the high-frequency branch assuming $r_b/a=1.2$, $r_p/a=1.4$ and $b/a=1.6$. Stability results are presented for several values of $s_e=\hat{\omega}_{pe}^2/\omega_{ce}^2$ ranging from $s_e=0$ to $s_e=0.5$, and for (a) $\ell=4$, (b) $\ell=8$, and (c) $\ell=12$.

Fig. 13 Plots of normalized real frequency $\mathrm{Re}\omega/\omega_{ce}$ and growth rate $\mathrm{Im}\omega/\omega_{ce}$ obtained from Eq. (48) assuming $\ell=8$, $r_b/a=1.2$, $r_p/a=1.4$ and $b/a=1.6$. Plots are versus (a) $\hat{\omega}_{pb}^2/\omega_{ce}^2$, for $\hat{n}_e/\hat{n}_b=0.5$, and (b) $\hat{n}_e/\hat{n}_b$, for $\hat{\omega}_{pb}^2/\omega_{ce}^2=0.4$. Both the high-frequency branch (labeled by 1) and the low-frequency branch (labeled by 2) are displayed.

Fig. 14 Plots of normalized real frequency $\mathrm{Re}\omega/\omega_{ce}$ and growth rate $\mathrm{Im}\omega/\omega_{ce}$ versus $\hat{\omega}_{pb}^2/\omega_{ce}^2$ obtained from Eq. (48) for $\ell=8$, $\hat{n}_e/\hat{n}_b=0.5$, $r_b/a=1.07$, $r_p/a=1.14$ and $b/a=1.21$. Both the high-frequency branch (labeled by 1) and the low-frequency branch (labeled by 2) are displayed.

Fig. 15 Plots of normalized real frequency $\mathrm{Re}\omega/\omega_{ce}$ and growth rate $\mathrm{Im}\omega/\omega_{ce}$ versus $\Delta=(b-a)/a$ obtained from Eq. (48) for $\ell=8$, $\hat{n}_e/\hat{n}_b=0.5$, and (a) $\hat{\omega}_{pb}^2/\omega_{ce}^2=0.4$, and (b) $\hat{\omega}_{pb}^2/\omega_{ce}^2=0.7$. In Figs. 15(a) and 15(b) it is assumed that $(r_b-a)/a=\Delta/3$ and $(r_p-a)/a=2\Delta/3$. Both the high-frequency branch (labeled by 1) and the low-frequency branch (labeled by 2) are displayed.

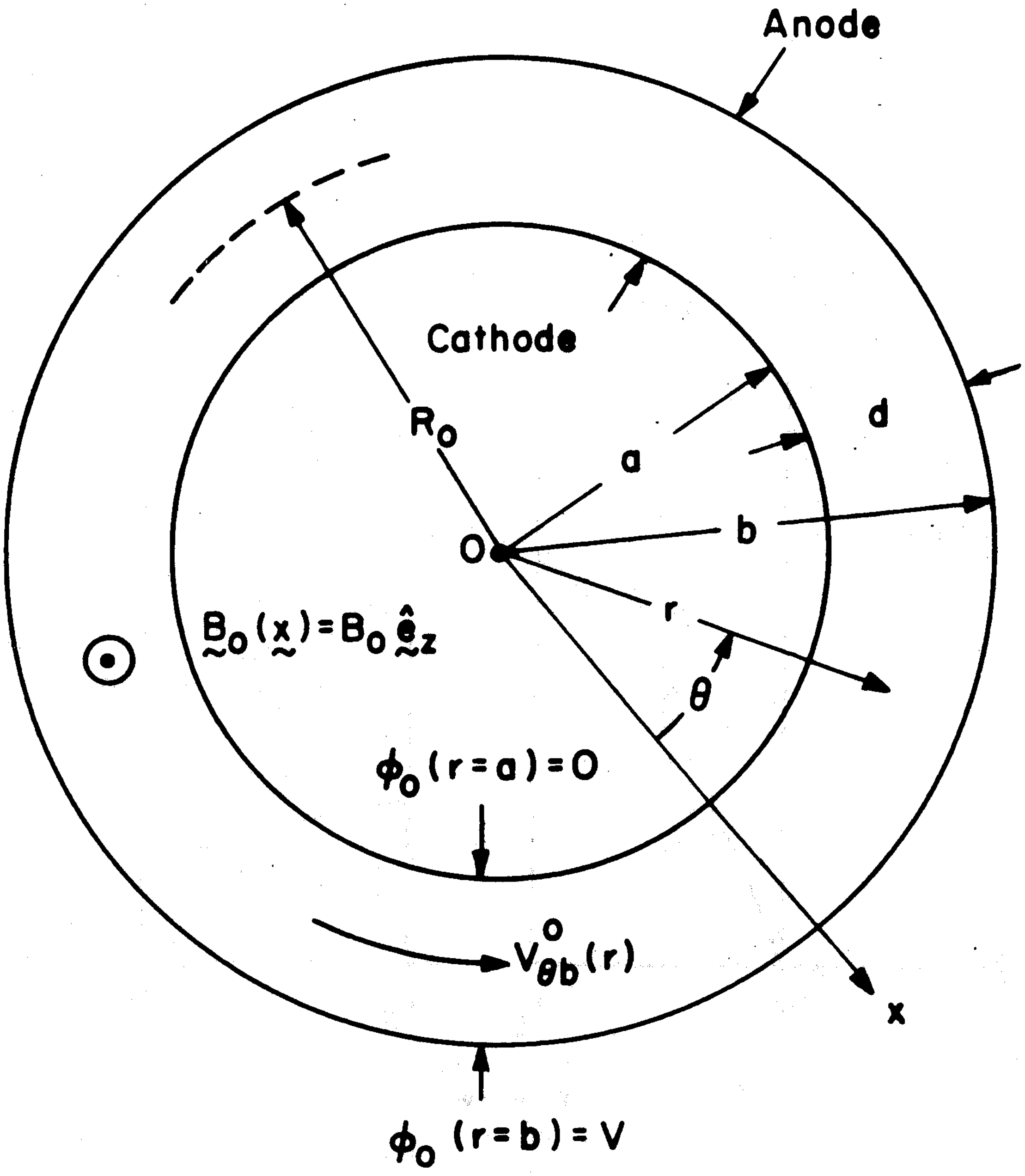
Anode
Cathode
R_0
a
b
d
O
r
θ
x
$\underset{\sim}{B}_0(\underset{\sim}{x}) = B_0\hat{\underset{\sim}{e}}_z$
$\phi_0(r=a)=0$
$V^0_{\theta b}(r)$
$\phi_0(r=b)=V$

Fig. 1

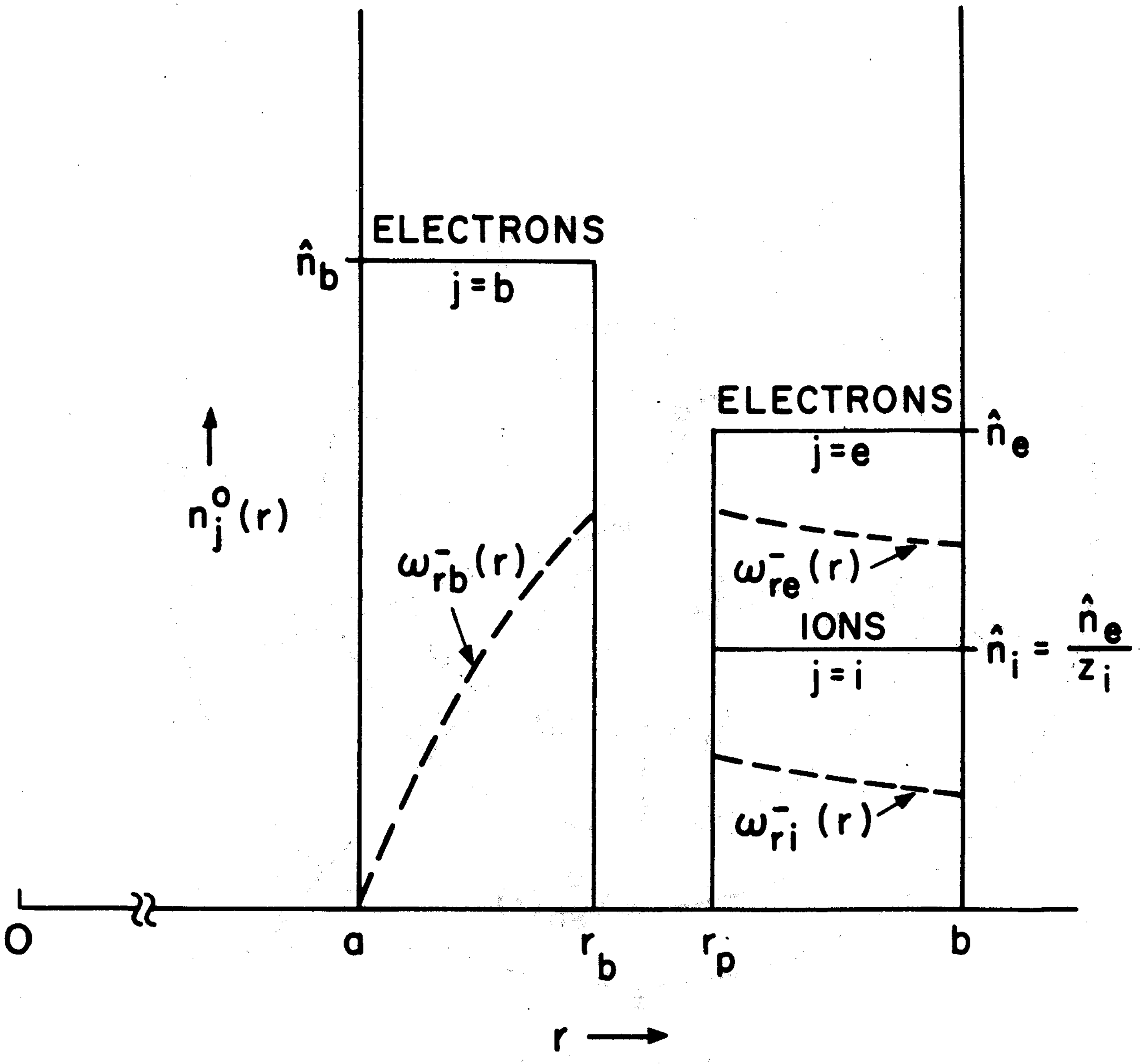
ELECTRONS
$\hat{n}_b$
j = b
$n_j^o(r)$
$\omega_{rb}^-(r)$
ELECTRONS
j = e
$\hat{n}_e$
$\omega_{re}^-(r)$
IONS
j = i
$\hat{n}_i = \frac{\hat{n}_e}{z_i}$
$\omega_{ri}^-(r)$
O
a
r_b
r_p
b
r

Fig. 2

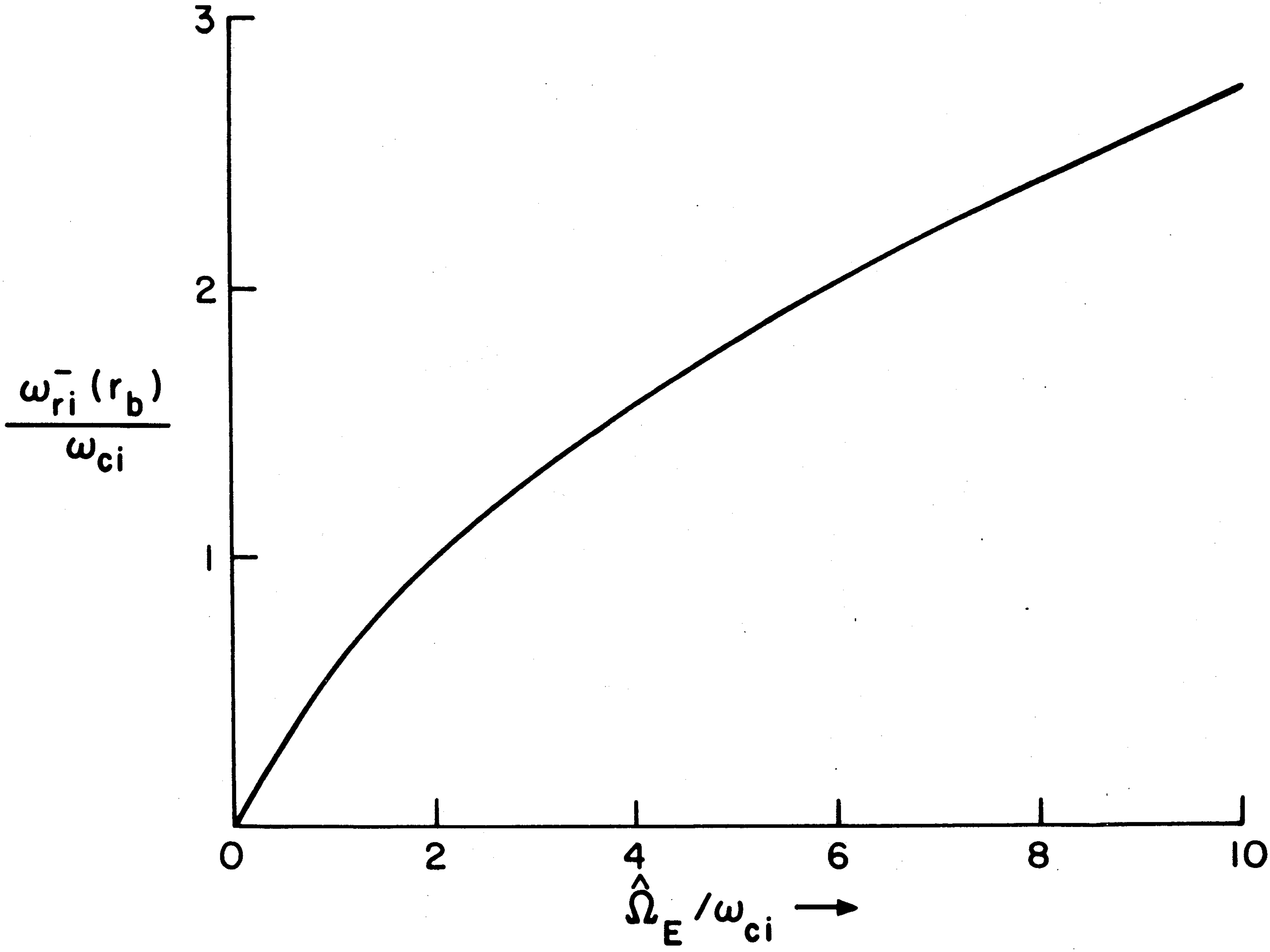

Fig. 3

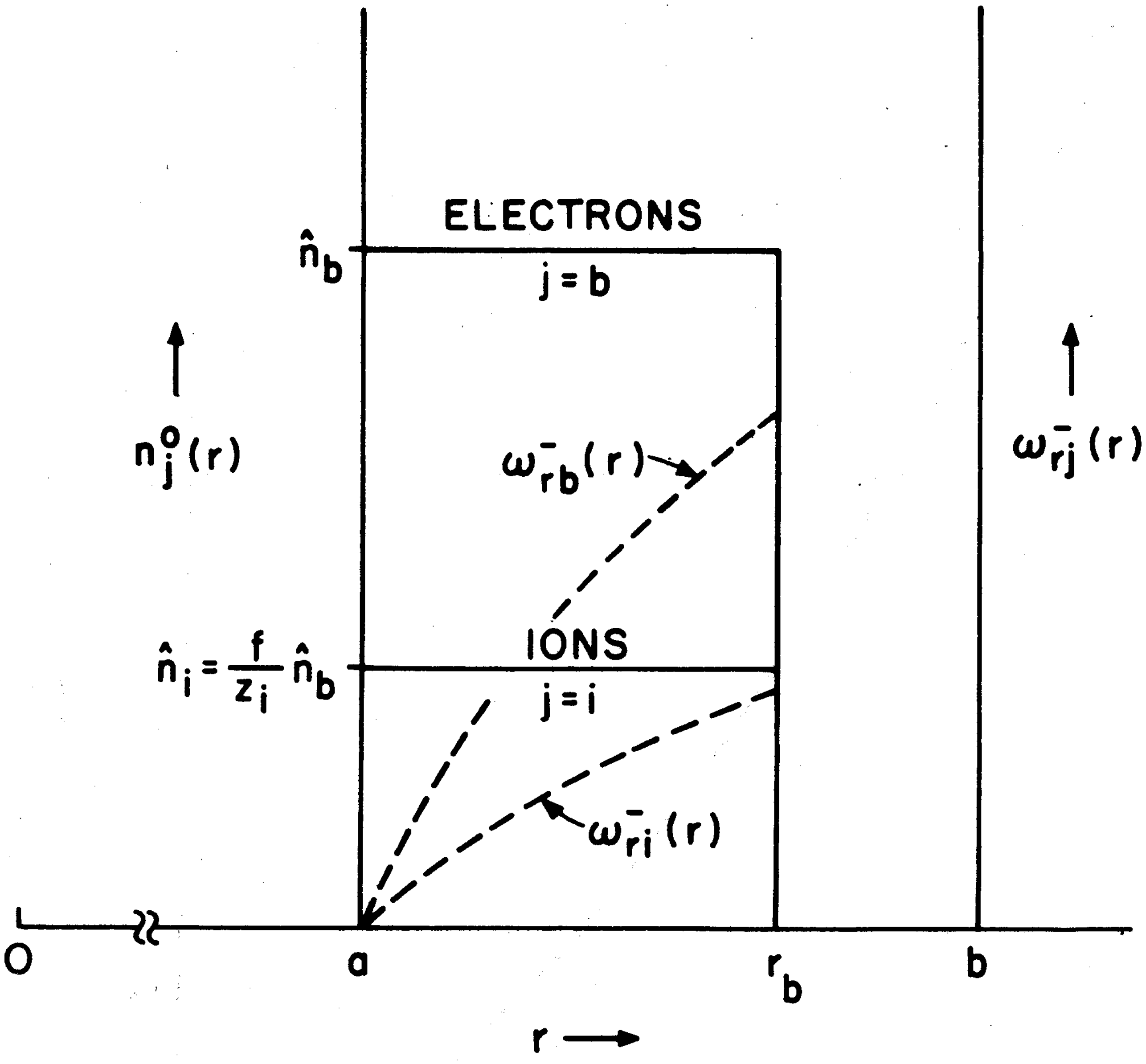
ELECTRONS
$\hat{n}_b$
$j = b$
$n_j^o(r)$
$\omega_{rb}^-(r)$
$\omega_{rj}^-(r)$
IONS
$\hat{n}_i = \frac{f}{z_i}\hat{n}_b$
$j = i$
$\omega_{ri}^-(r)$
O
a
r_b
b
r

Fig. 4

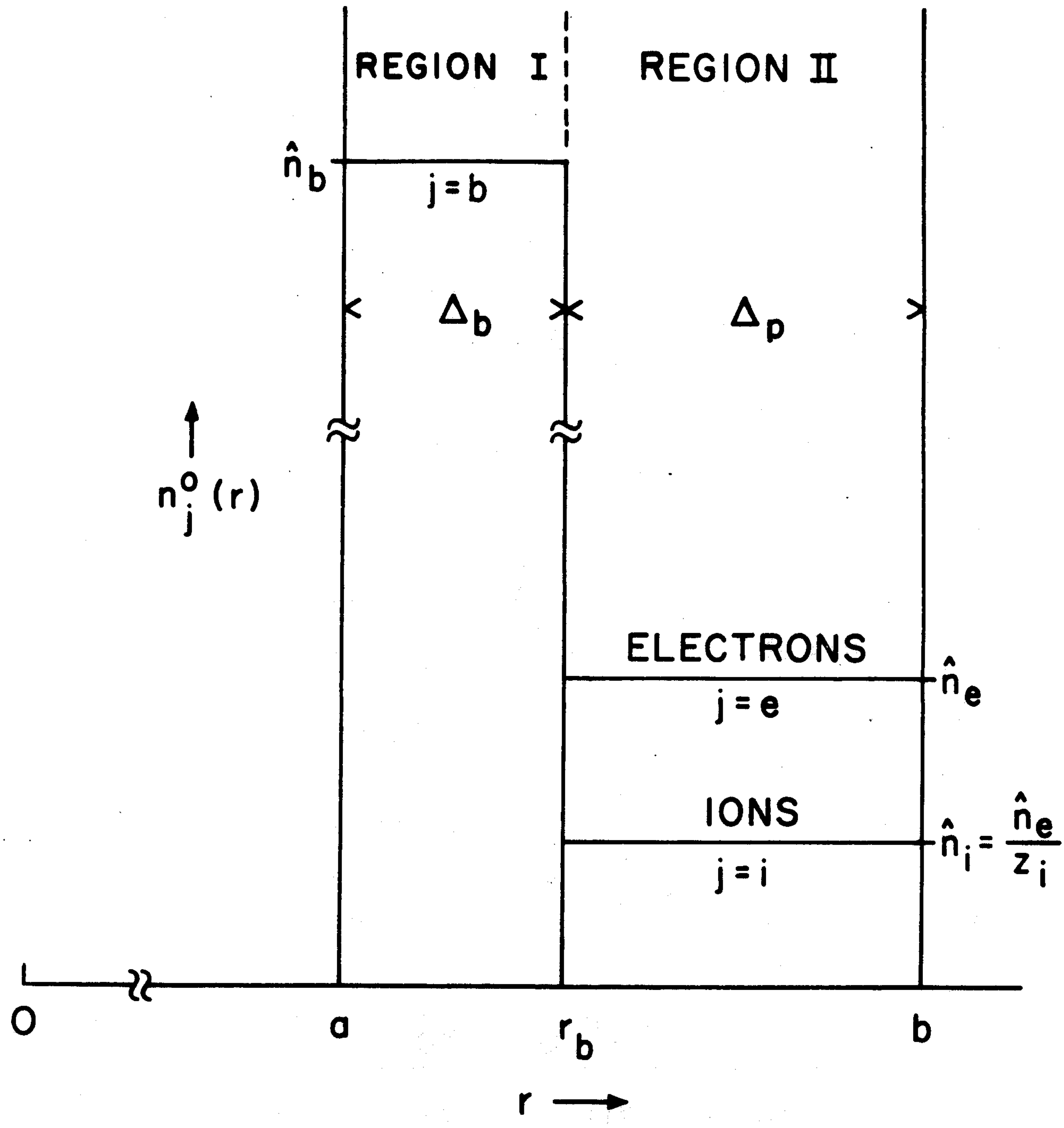
REGION I
REGION II
$\hat{n}_b$
$j=b$
Δ_b
Δ_p
$n_j^o(r)$
ELECTRONS
$j=e$
$\hat{n}_e$
IONS
$j=i$
$\hat{n}_i = \frac{\hat{n}_e}{z_i}$
O
a
r_b
b
r

Fig. 5

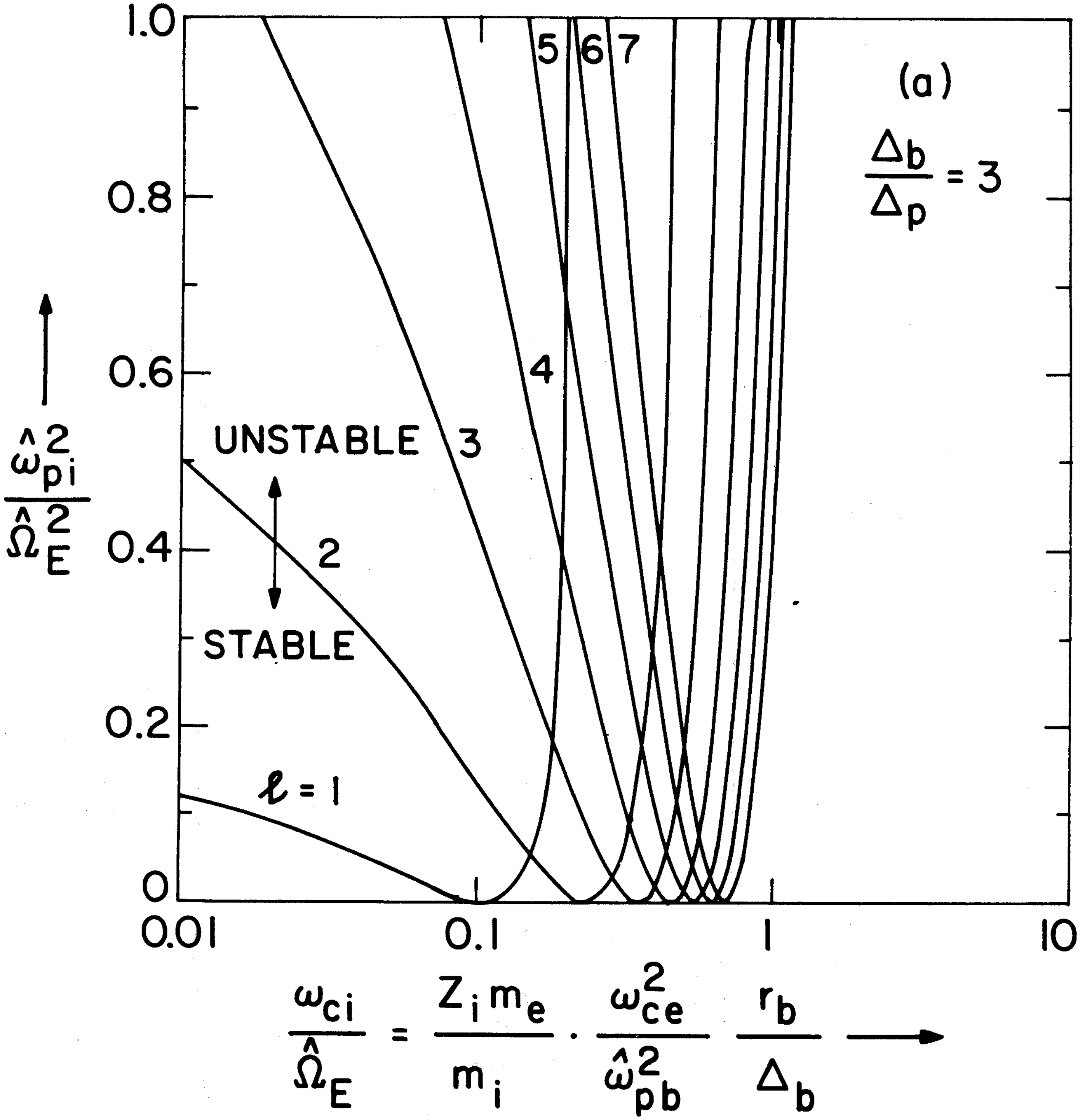
1.0
0.8
0.6
0.4
0.2
0
$\frac{\hat{\omega}_{pi}^2}{\hat{\Omega}_E^2}$
UNSTABLE
STABLE
$\ell = 1$
2
3
4
5
6
7
(a)
$\frac{\Delta_b}{\Delta_p} = 3$
0.01
0.1
1
10
$\frac{\omega_{ci}}{\hat{\Omega}_E} = \frac{Z_i m_e}{m_i} \cdot \frac{\omega_{ce}^2}{\hat{\omega}_{pb}^2} \frac{r_b}{\Delta_b}$

Fig. 6(a)

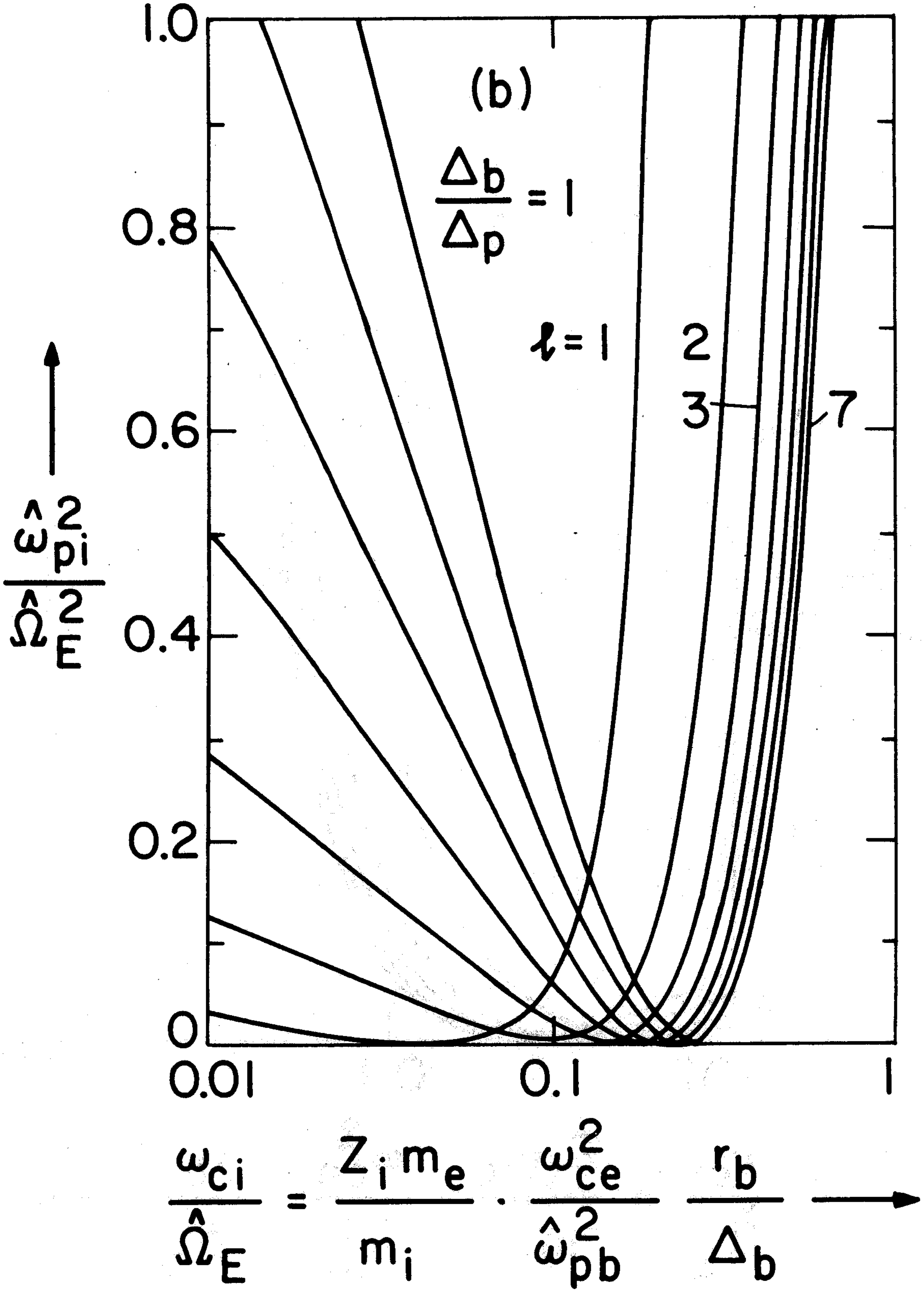
1.0
0.8
0.6
0.4
0.2
0
(b)
$\frac{\Delta_b}{\Delta_p} = 1$
$\ell = 1$
2
3
7
$\frac{\hat{\omega}_{pi}^2}{\hat{\Omega}_E^2}$
0.01
0.1
1
$\frac{\omega_{ci}}{\hat{\Omega}_E} = \frac{Z_i m_e}{m_i} \cdot \frac{\omega_{ce}^2}{\hat{\omega}_{pb}^2} \frac{r_b}{\Delta_b}$

Fig. 6(b)

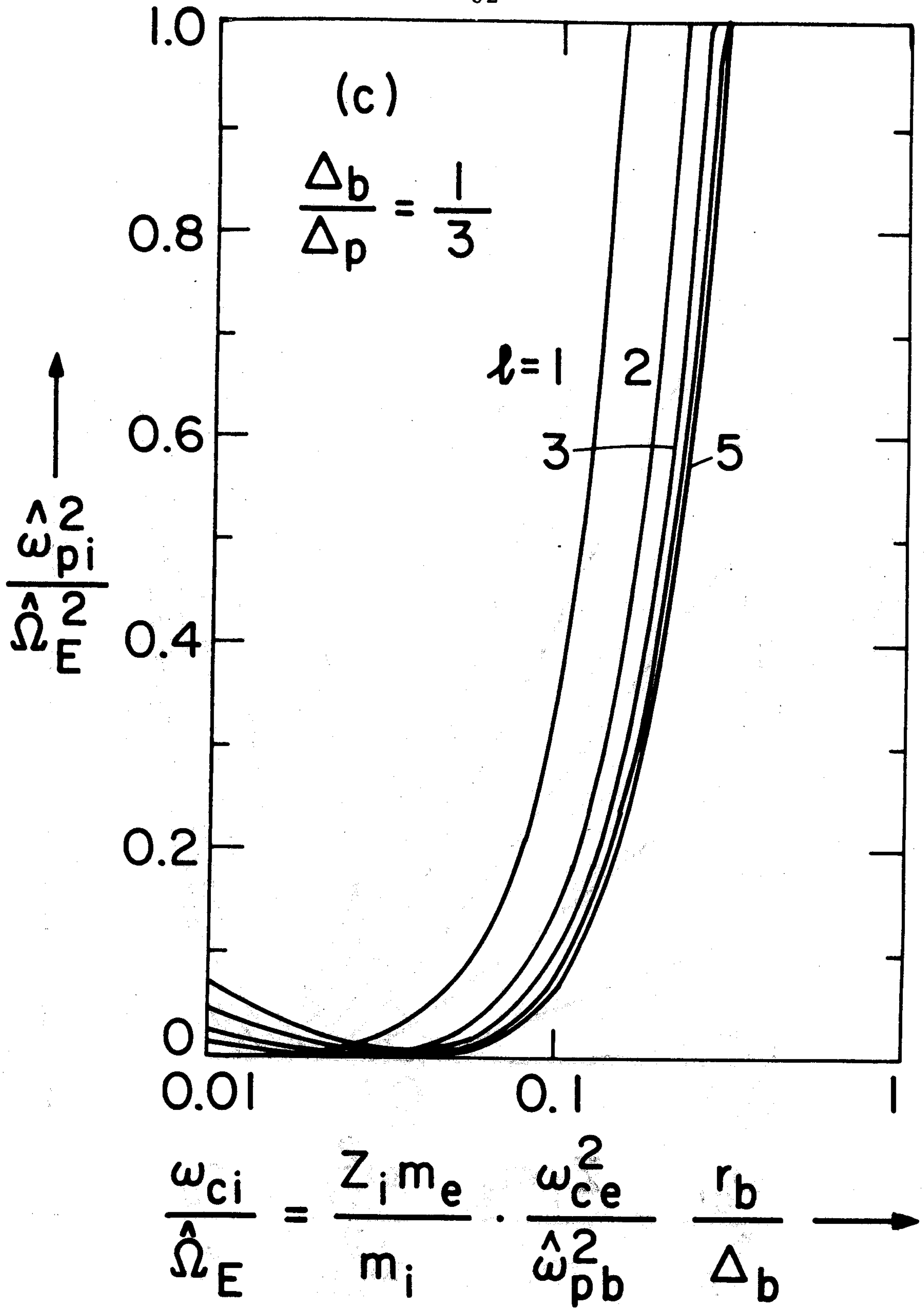
(c)
$\frac{\Delta_b}{\Delta_p} = \frac{1}{3}$
$\ell = 1$
2
3
5
1.0
0.8
0.6
0.4
0.2
0
$\frac{\hat{\omega}_{pi}^2}{\hat{\Omega}_E^2}$
0.01
0.1
1
$\frac{\omega_{ci}}{\hat{\Omega}_E} = \frac{Z_i m_e}{m_i} \cdot \frac{\omega_{ce}^2}{\hat{\omega}_{pb}^2} \frac{r_b}{\Delta_b}$

Fig. 6(c)

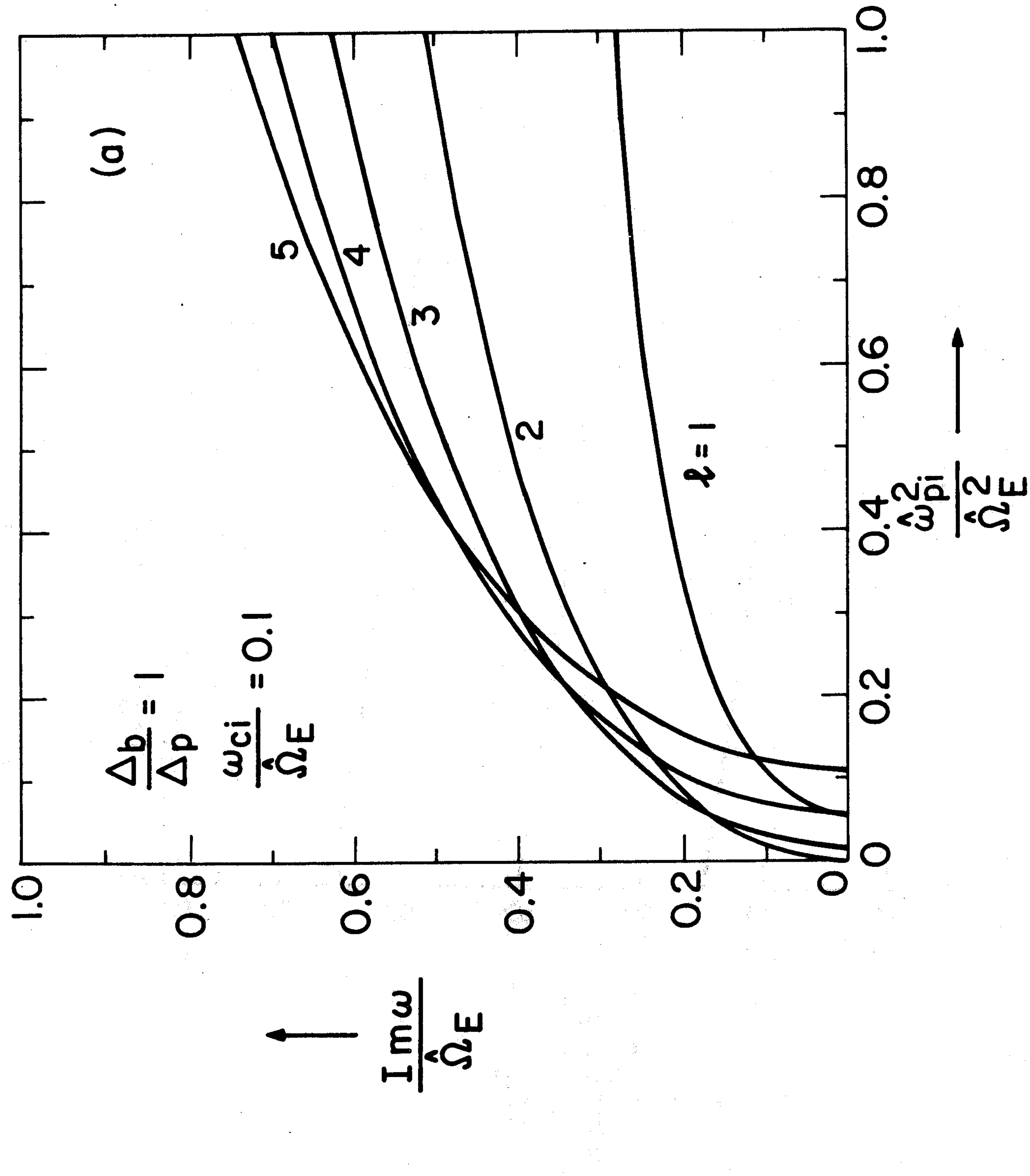
(a)
$\frac{\Delta_b}{\Delta_p} = 1$
$\frac{\omega_{ci}}{\hat{\Omega}_E} = 0.1$
$\ell = 1$
2
3
4
5
$\frac{\mathrm{Im}\,\omega}{\hat{\Omega}_E}$
$\frac{\hat{\omega}_{pi}^2}{\hat{\Omega}_E^2}$
0
0.2
0.4
0.6
0.8
1.0
0
0.2
0.4
0.6
0.8
1.0

Fig. 7(a)

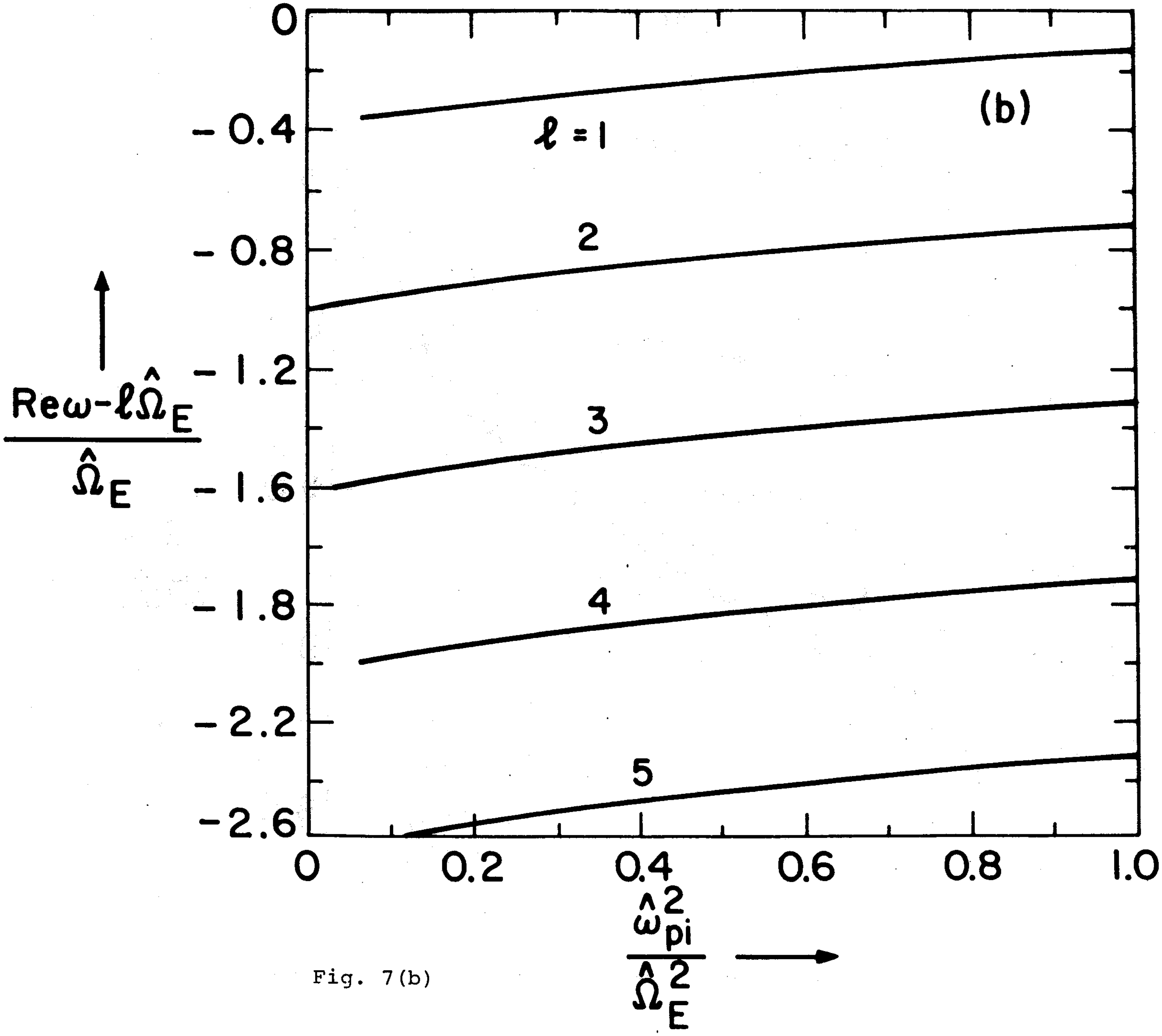
(b)
$\ell = 1$
2
3
4
5
0
- 0.4
- 0.8
- 1.2
- 1.6
- 1.8
- 2.2
- 2.6
$\frac{Re\omega - \ell\hat{\Omega}_E}{\hat{\Omega}_E}$
0
0.2
0.4
0.6
0.8
1.0
$\frac{\hat{\omega}_{pi}^2}{\hat{\Omega}_E^2}$

Fig. 7(b)

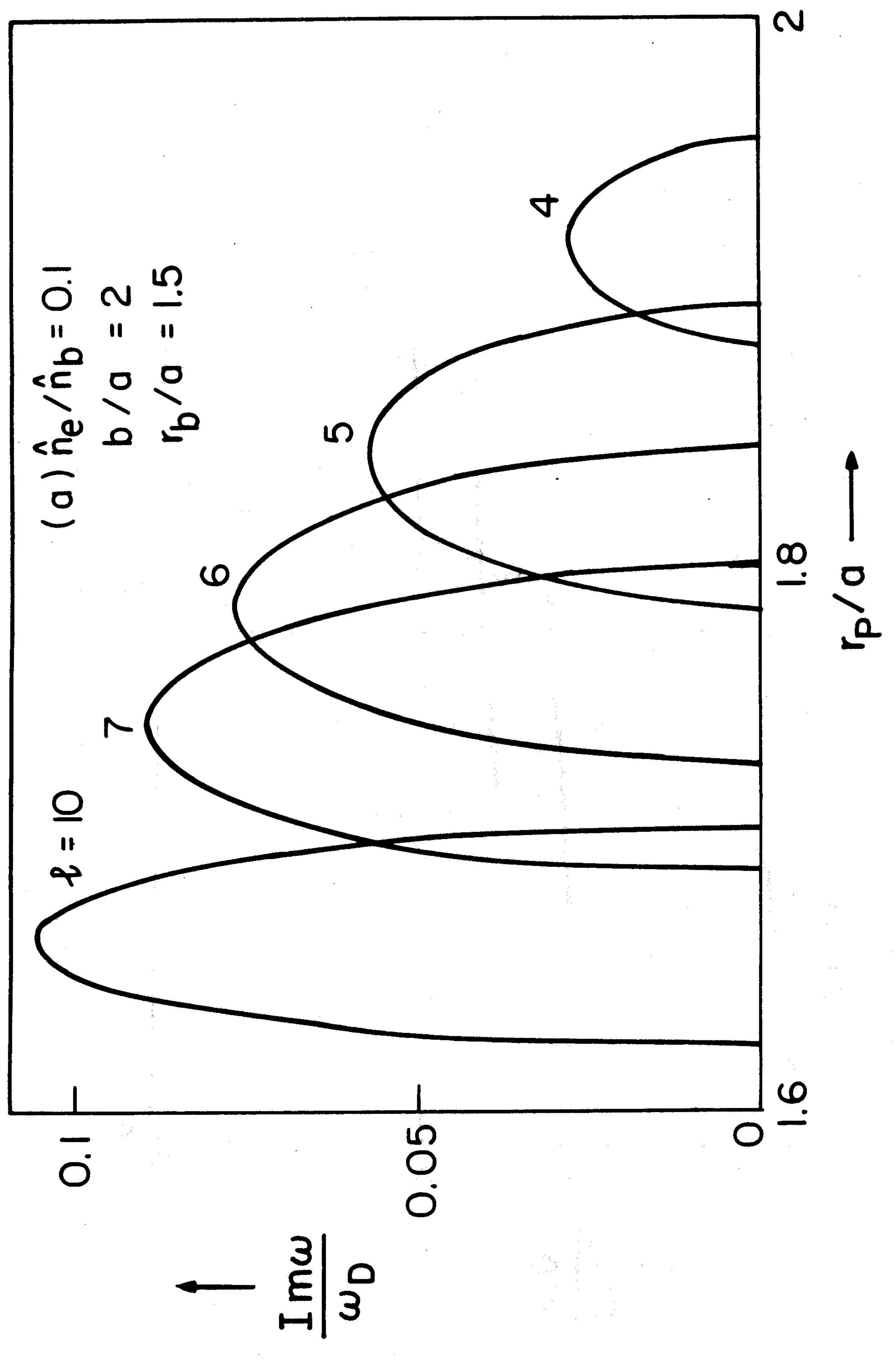
$\frac{\mathrm{Im}\,\omega}{\omega_D}$
0.1
0.05
0
1.6
1.8
2
r_p/a
$\ell = 10$
7
6
5
4
(a) $\hat{n}_e/\hat{n}_b = 0.1$
$b/a = 2$
$r_b/a = 1.5$

Fig. 8(a)

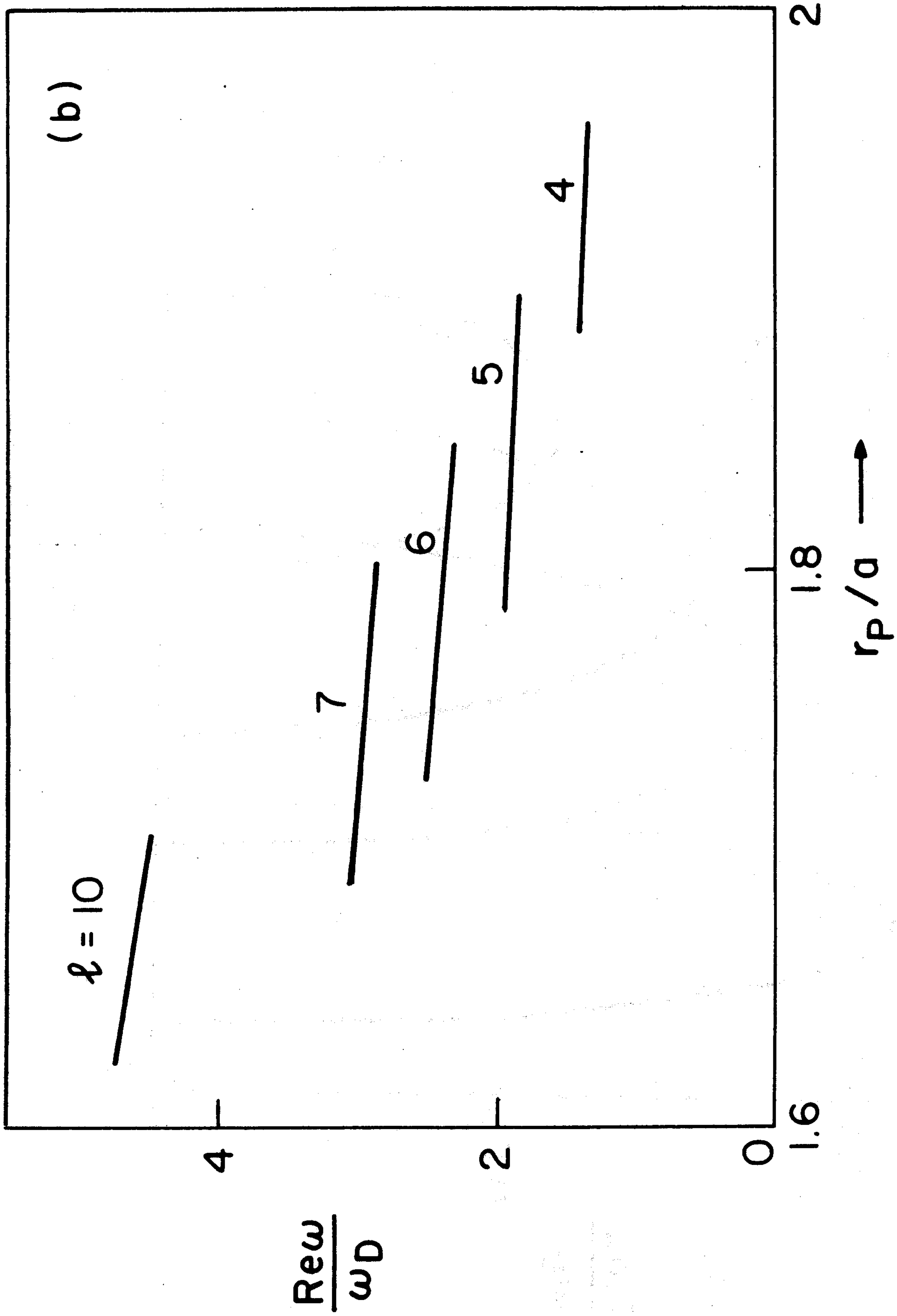

Fig. 8(b)

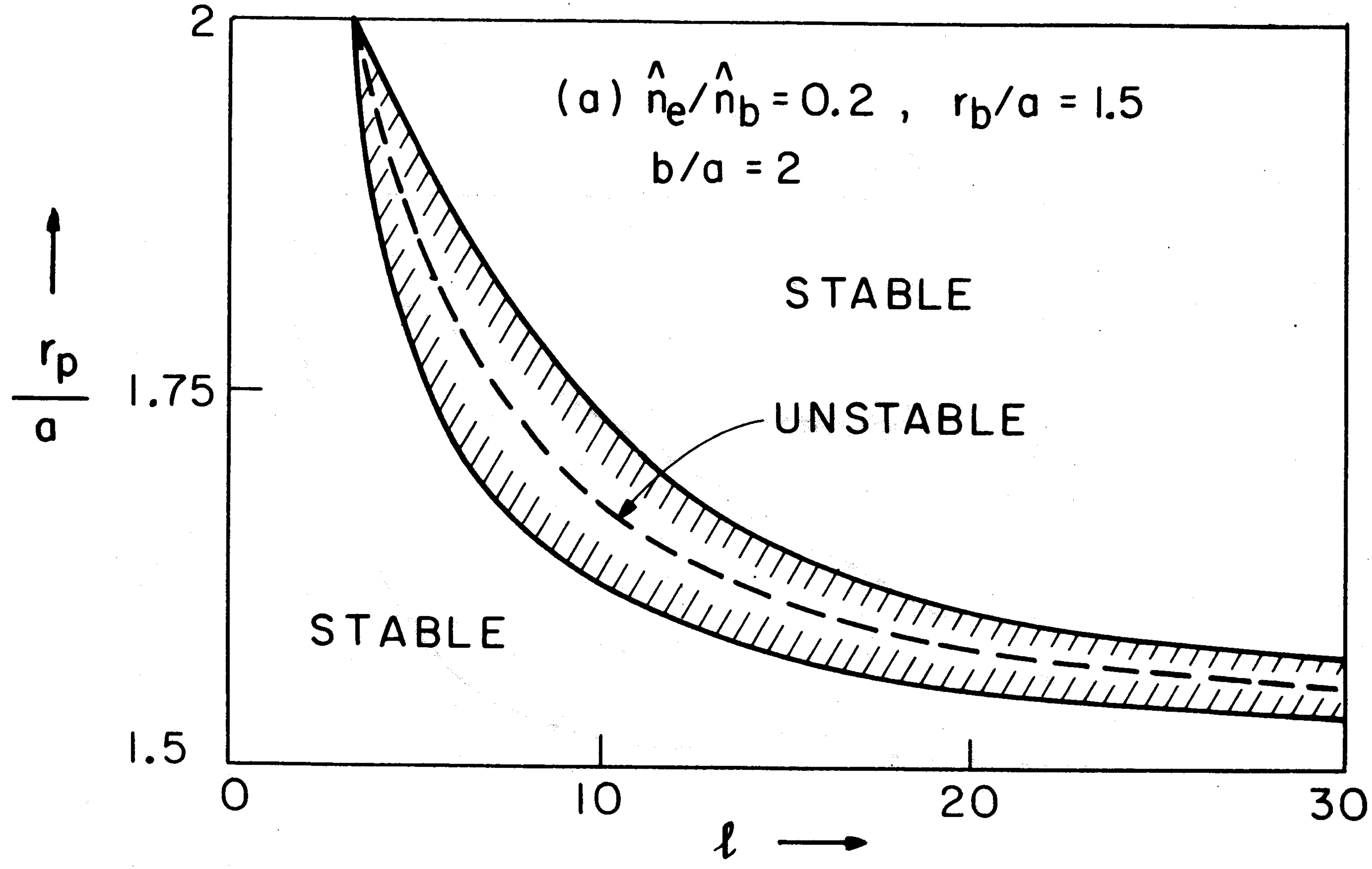
(a) $\hat{n}_e/\hat{n}_b = 0.2$, $r_b/a = 1.5$
$b/a = 2$
STABLE
UNSTABLE
STABLE
$\frac{r_p}{a}$
2
1.75
1.5
0
10
20
30
ℓ

Fig 9(a)

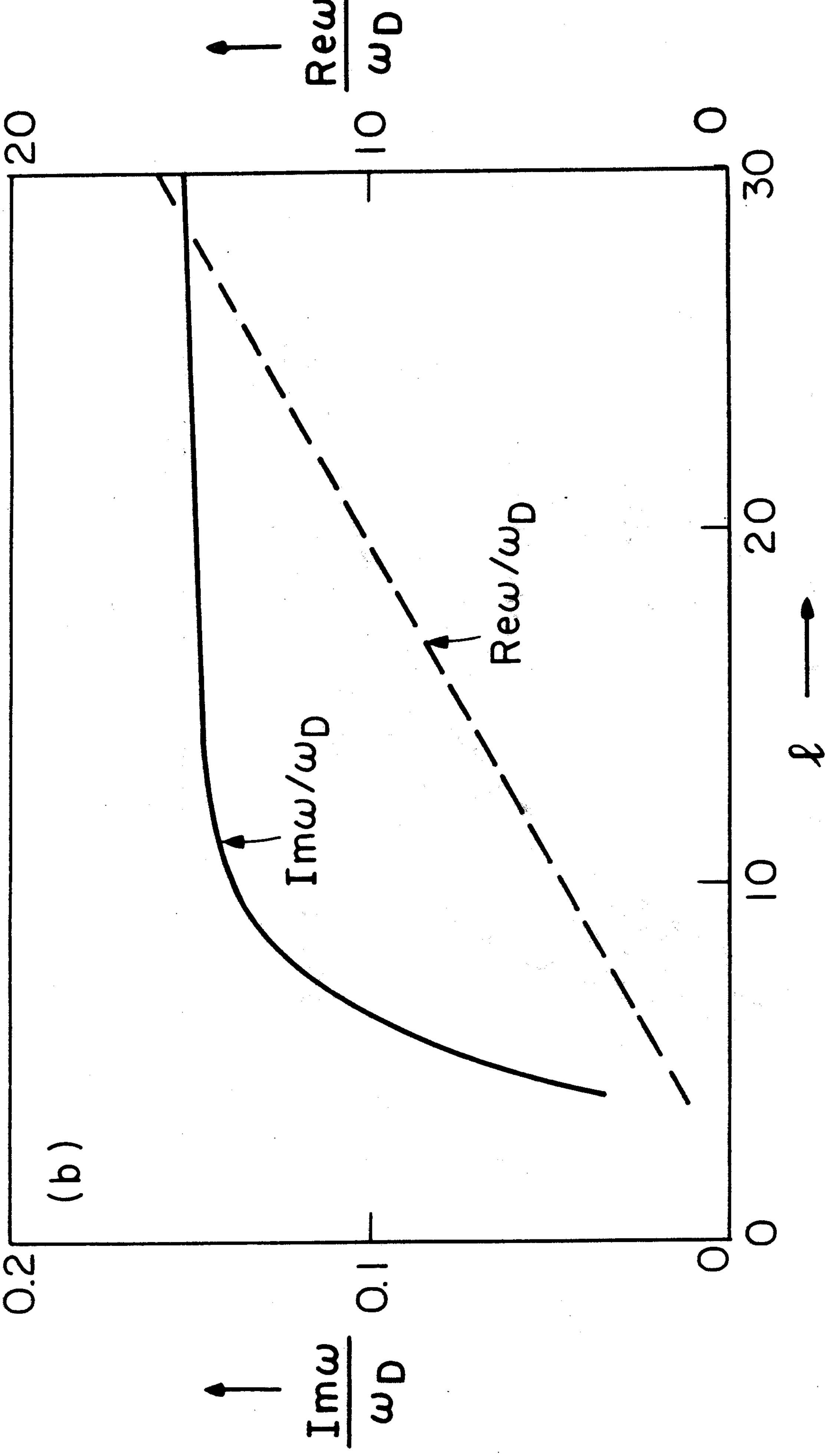

Fig. 9(b)

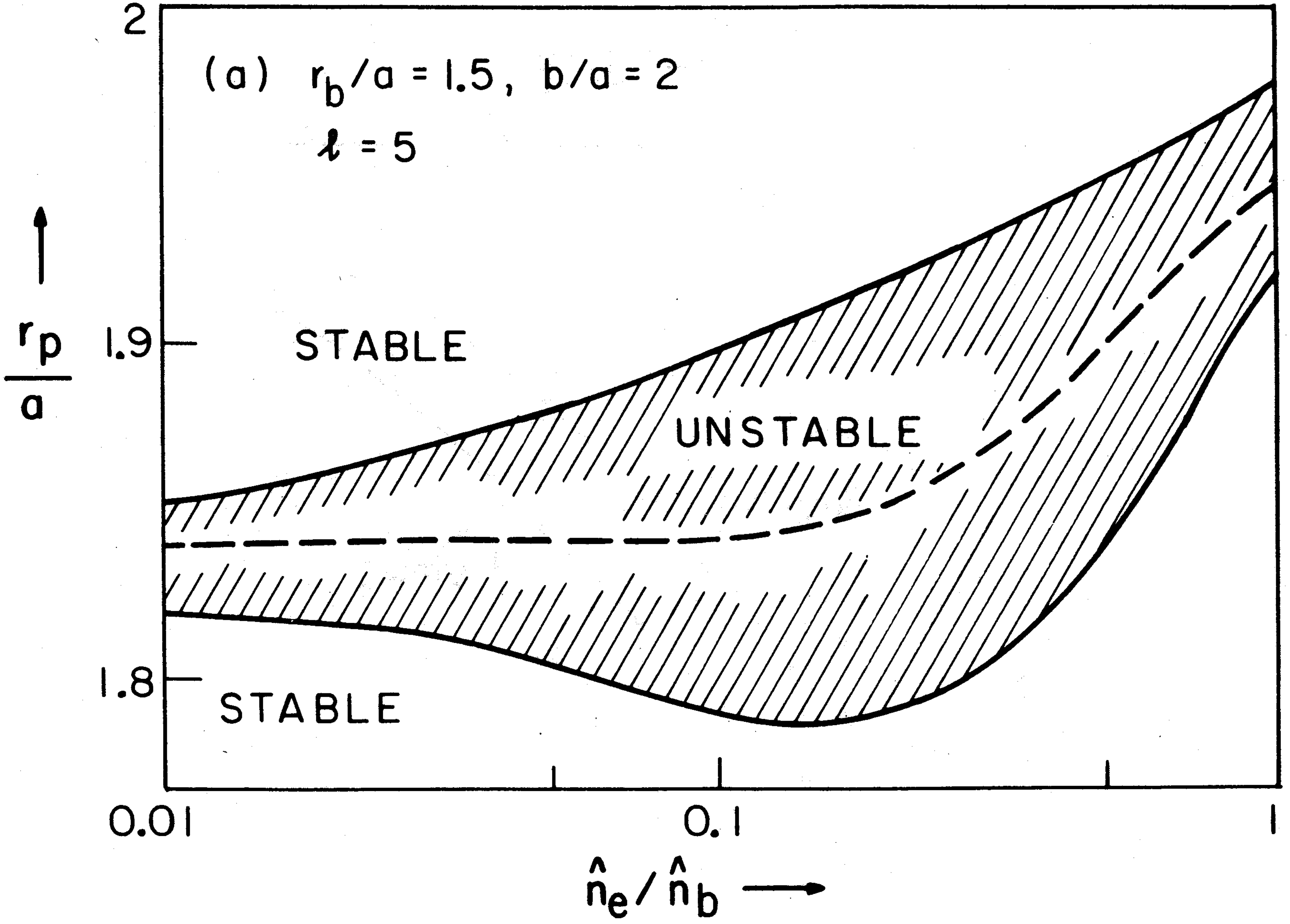
(a) $r_b/a = 1.5$, $b/a = 2$
$\ell = 5$
r_p/a
2
1.9
1.8
STABLE
UNSTABLE
STABLE
0.01
0.1
1
$\hat{n}_e/\hat{n}_b$

Fig. 10(a)

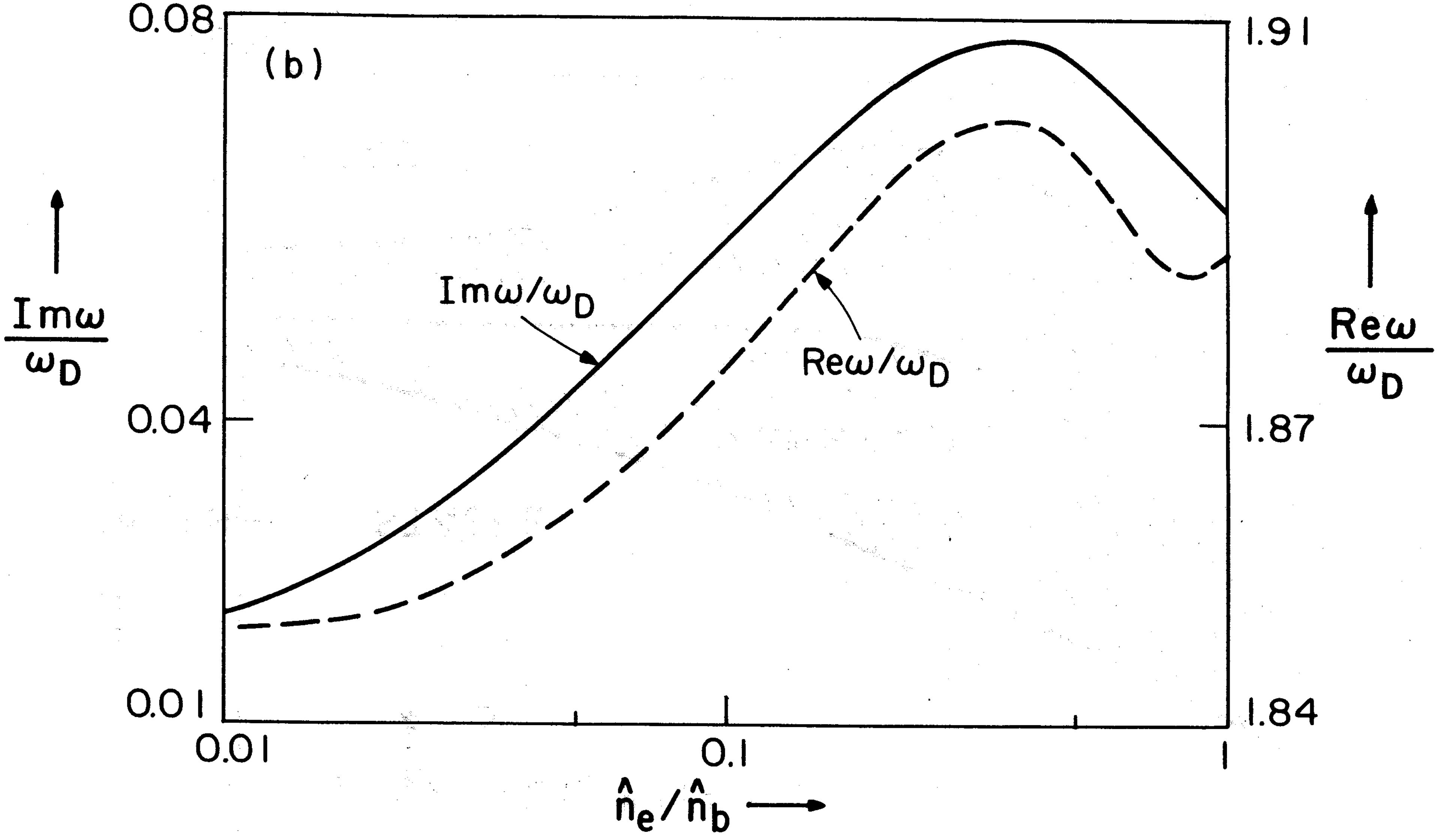
(b)
$\frac{Im\omega}{\omega_D}$
0.08
0.04
0.01
$Re\omega/\omega_D$
$Im\omega/\omega_D$
$\frac{Re\omega}{\omega_D}$
1.91
1.87
1.84
0.01
0.1
1
$\hat{n}_e/\hat{n}_b$

Fig. 10(b)

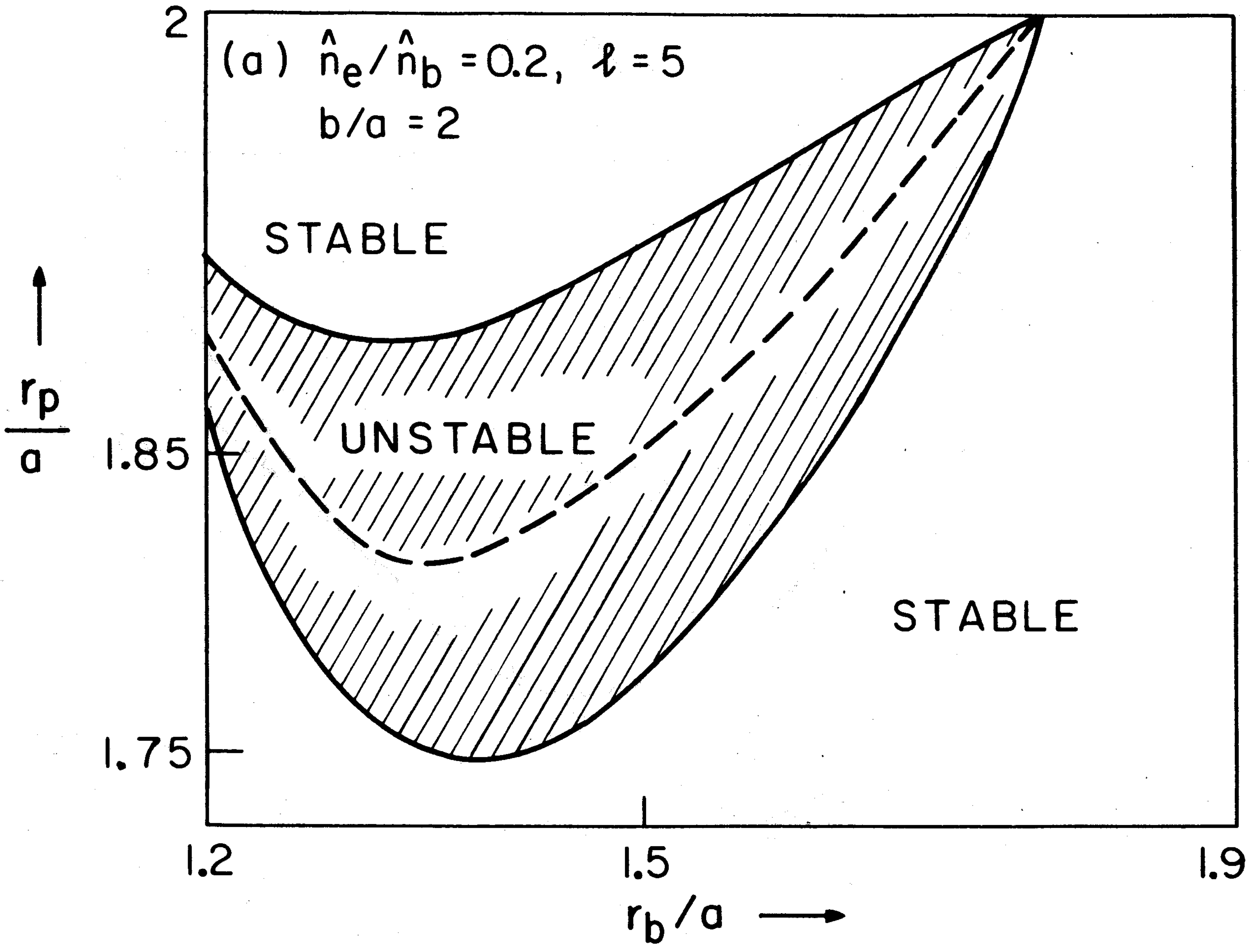
(a) $\hat{n}_e/\hat{n}_b = 0.2$, $\ell = 5$
$b/a = 2$
STABLE
UNSTABLE
STABLE
r_p/a
2
1.85
1.75
1.2
1.5
1.9
r_b/a

Fig. 11(a)

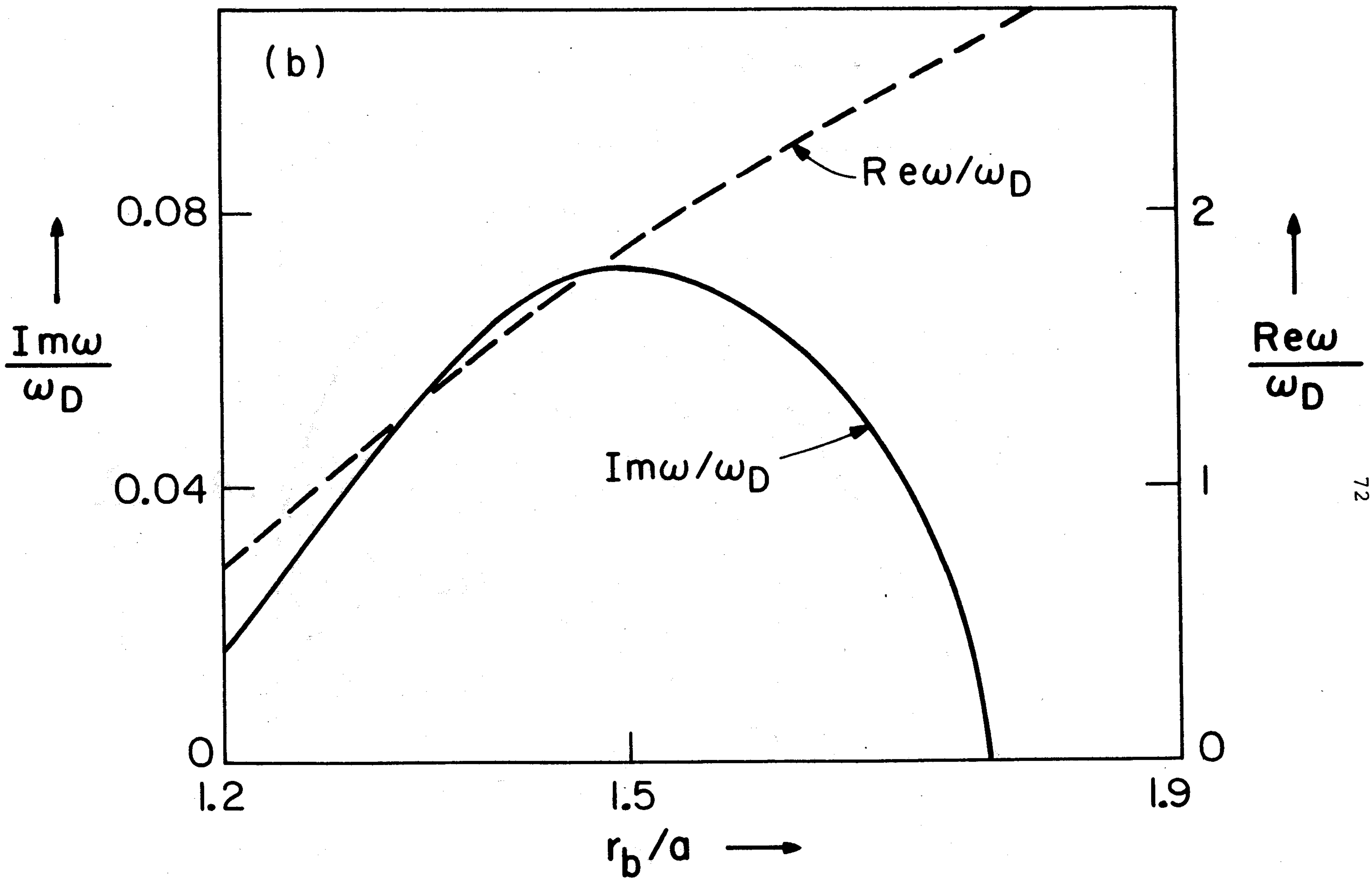
(b)
0.08
0.04
0
$\frac{Im\omega}{\omega_D}$
2
1
0
$\frac{Re\omega}{\omega_D}$
$Re\omega/\omega_D$
$Im\omega/\omega_D$
1.2
1.5
1.9
r_b/a

Fig. 11(b)

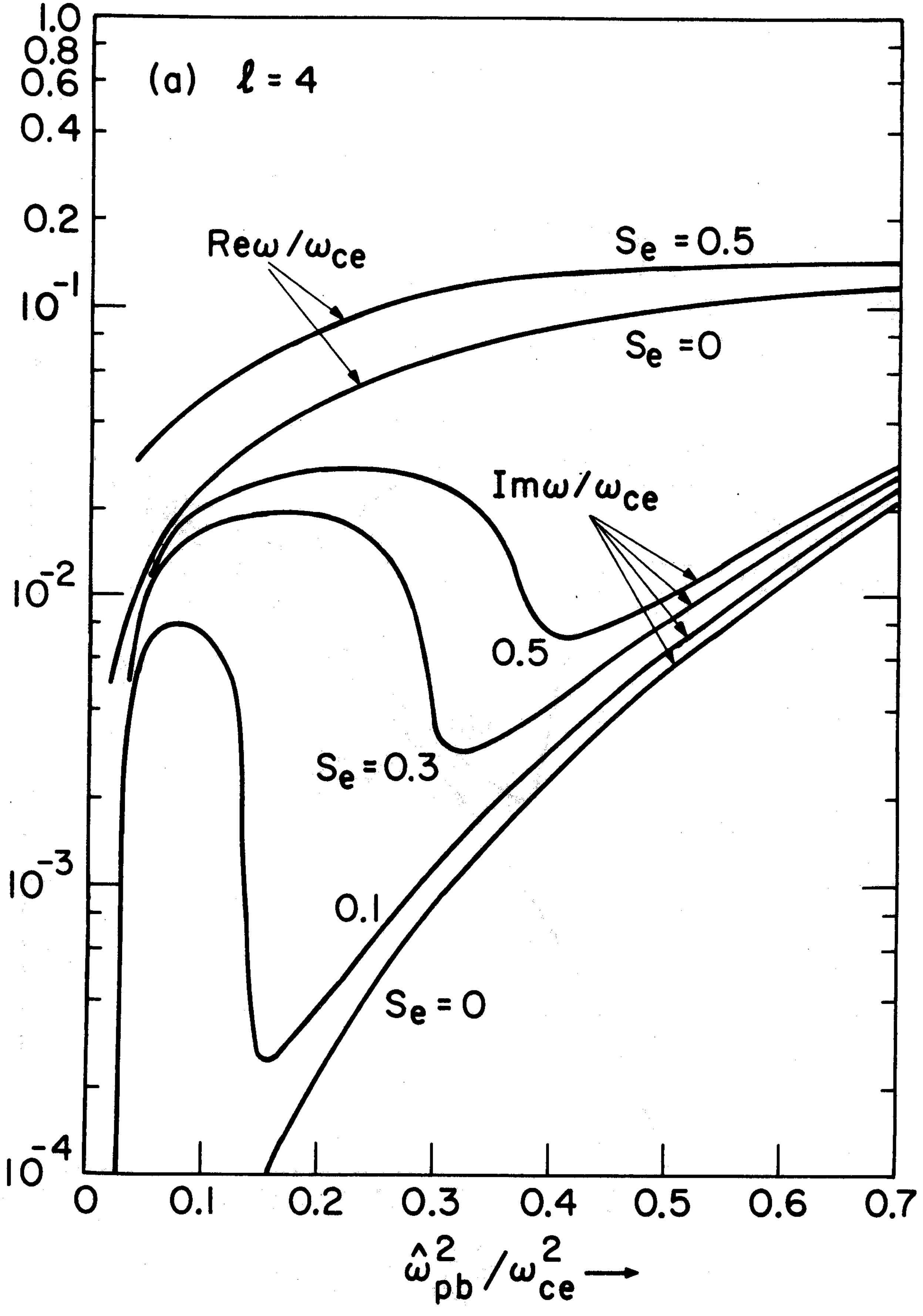
(a) $\ell = 4$
$Re\omega/\omega_{ce}$
$S_e = 0.5$
$S_e = 0$
$Im\omega/\omega_{ce}$
0.5
$S_e = 0.3$
0.1
$S_e = 0$
1.0
0.8
0.6
0.4
0.2
10^{-1}
10^{-2}
10^{-3}
10^{-4}
0
0.1
0.2
0.3
0.4
0.5
0.6
0.7
$\hat{\omega}_{pb}^2/\omega_{ce}^2 \rightarrow$

Fig. 12(a)

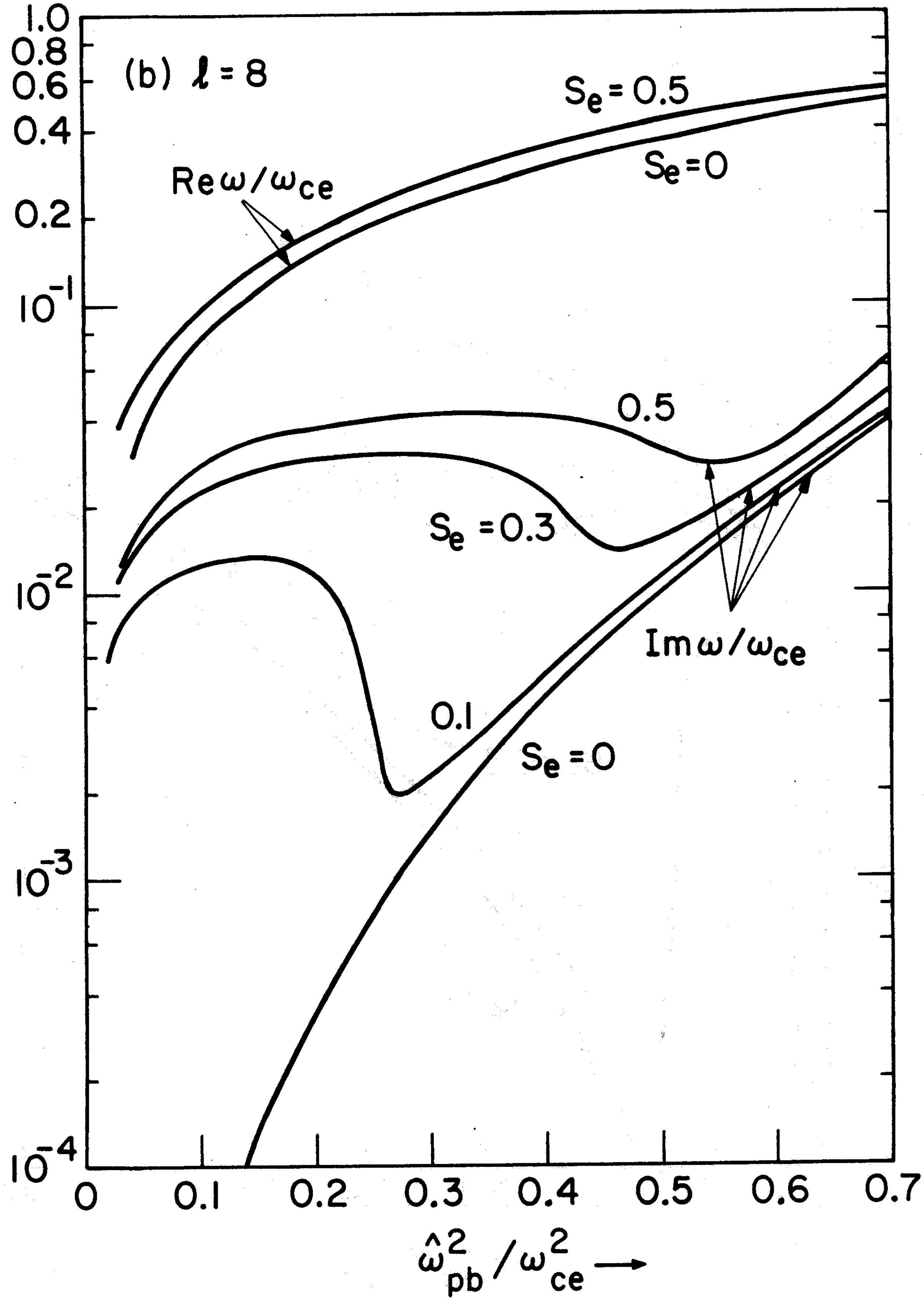
(b) $l = 8$
$S_e = 0.5$
$S_e = 0$
$\mathrm{Re}\,\omega/\omega_{ce}$
0.5
$S_e = 0.3$
0.1
$S_e = 0$
$\mathrm{Im}\,\omega/\omega_{ce}$
1.0
0.8
0.6
0.4
0.2
10^{-1}
10^{-2}
10^{-3}
10^{-4}
0
0.1
0.2
0.3
0.4
0.5
0.6
0.7
$\hat{\omega}_{pb}^2/\omega_{ce}^2 \rightarrow$

Fig. 12(b)

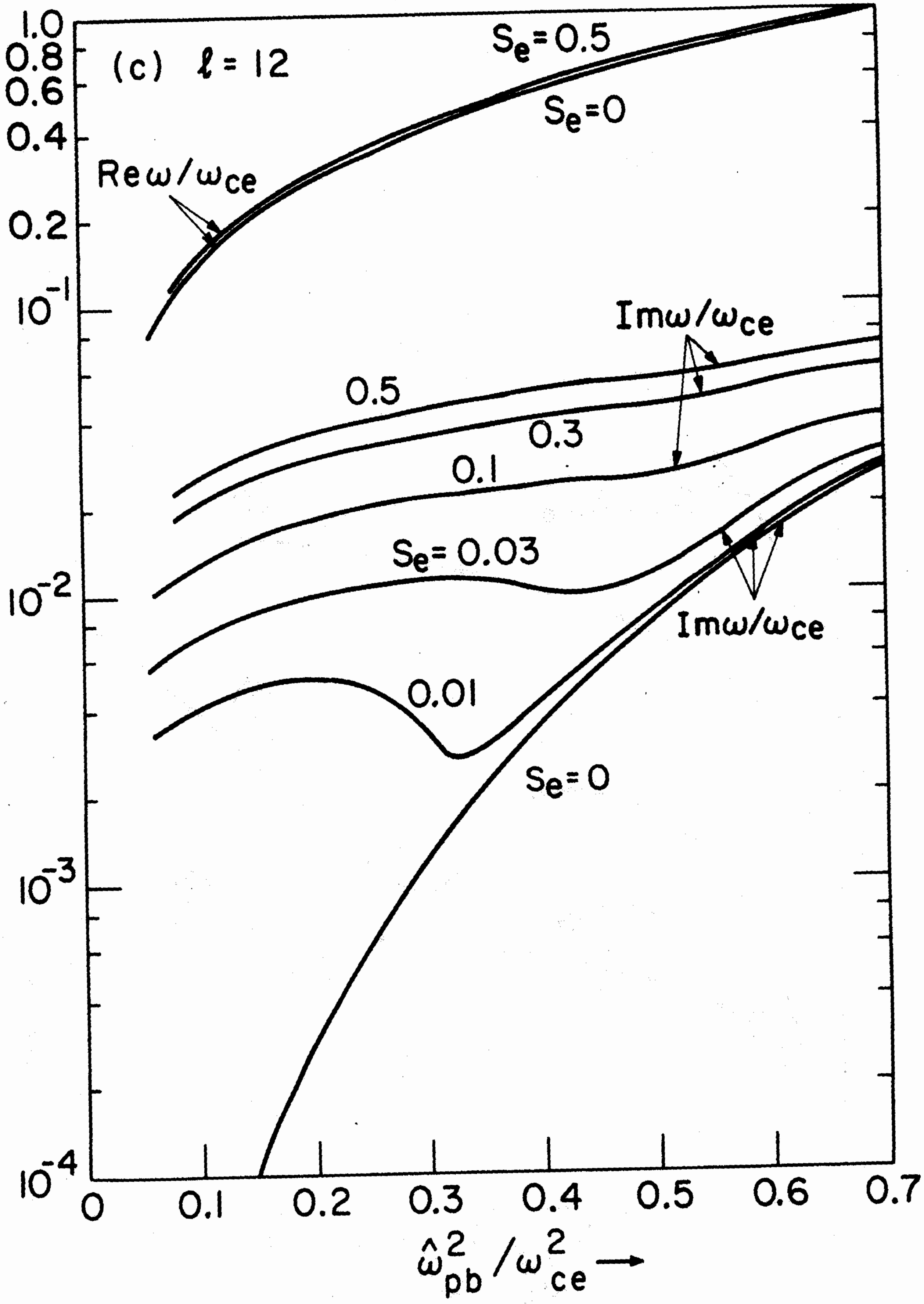
(c) ℓ = 12
S_e=0.5
S_e=0
Reω/ω_ce
Imω/ω_ce
0.5
0.3
0.1
S_e= 0.03
0.01
S_e= 0
Imω/ω_ce
1.0
0.8
0.6
0.4
0.2
10^{-1}
10^{-2}
10^{-3}
10^{-4}
0
0.1
0.2
0.3
0.4
0.5
0.6
0.7
$\hat{\omega}_{pb}^2/\omega_{ce}^2$ →

Fig. 12(c)

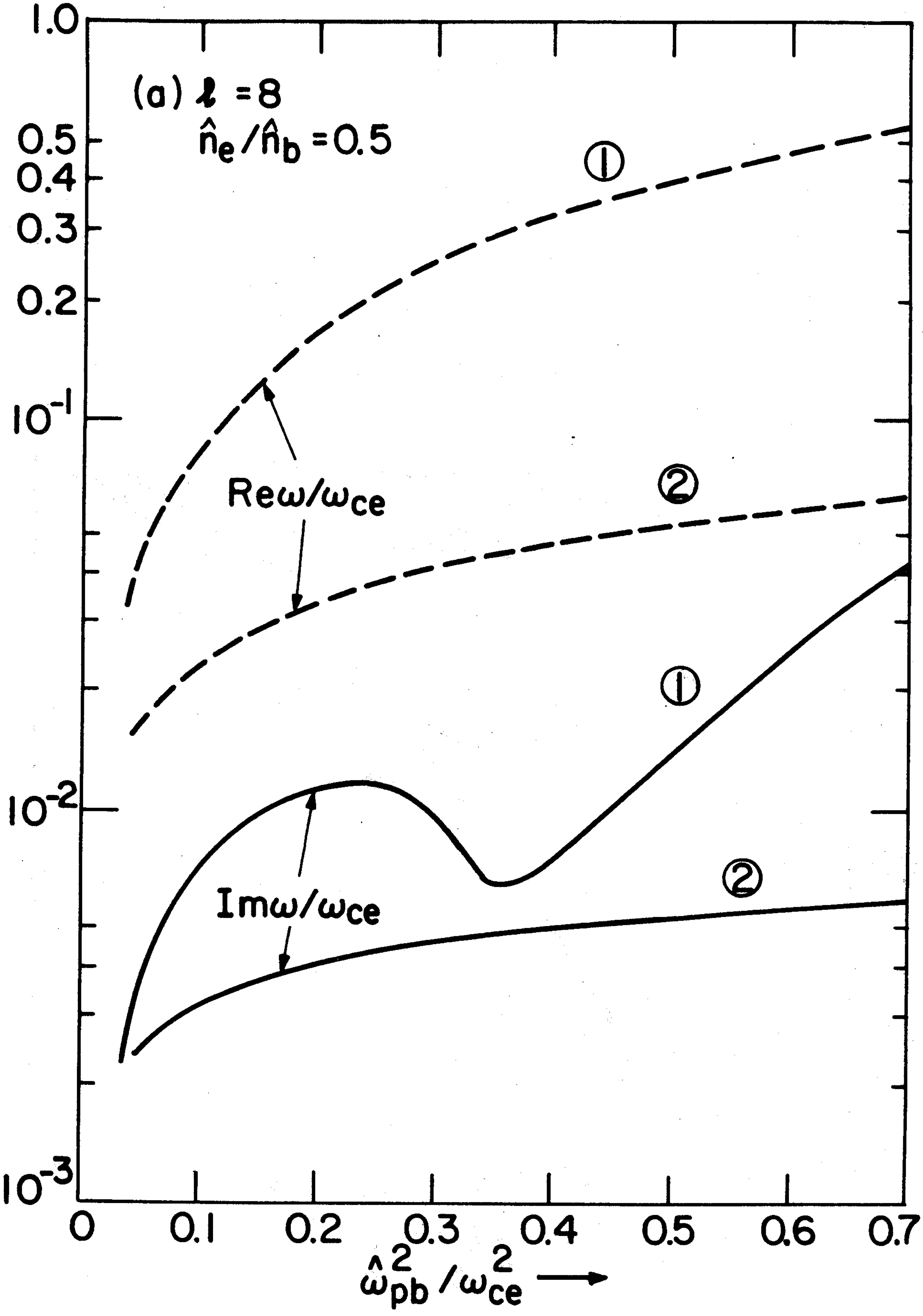
(a) $\ell = 8$
$\hat{n}_e/\hat{n}_b = 0.5$
①
②
①
②
$\mathrm{Re}\,\omega/\omega_{ce}$
$\mathrm{Im}\,\omega/\omega_{ce}$
1.0
0.5
0.4
0.3
0.2
10^{-1}
10^{-2}
10^{-3}
0
0.1
0.2
0.3
0.4
0.5
0.6
0.7
$\hat{\omega}_{pb}^2/\omega_{ce}^2$ →

Fig. 13(a)

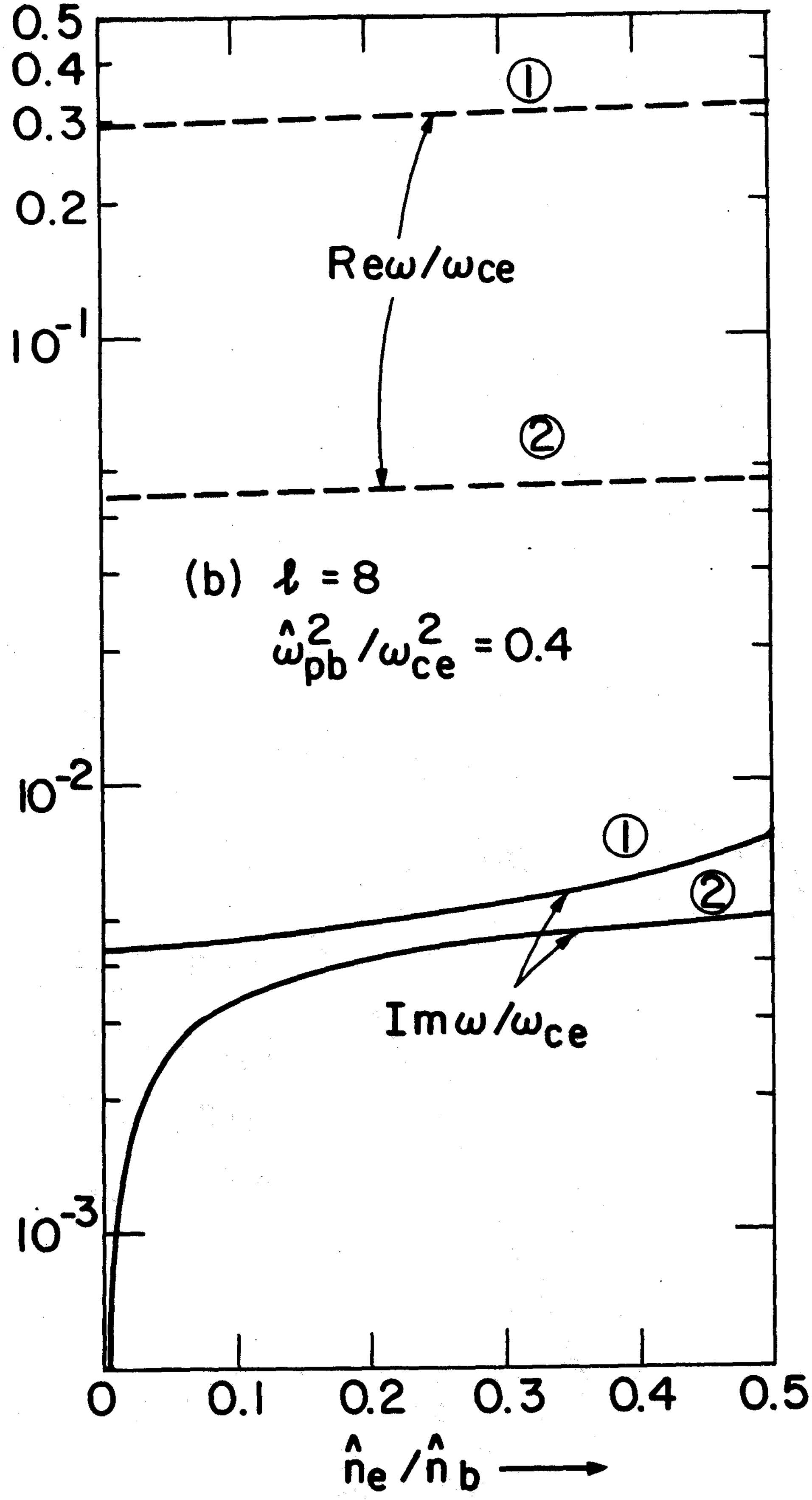
0.5
0.4
0.3
0.2
10^{-1}
10^{-2}
10^{-3}
①
②
$\mathrm{Re}\,\omega/\omega_{ce}$
(b) $\ell = 8$
$\hat{\omega}_{pb}^2/\omega_{ce}^2 = 0.4$
①
②
$\mathrm{Im}\,\omega/\omega_{ce}$
0
0.1
0.2
0.3
0.4
0.5
$\hat{n}_e/\hat{n}_b$ →

Fig. 13(b)

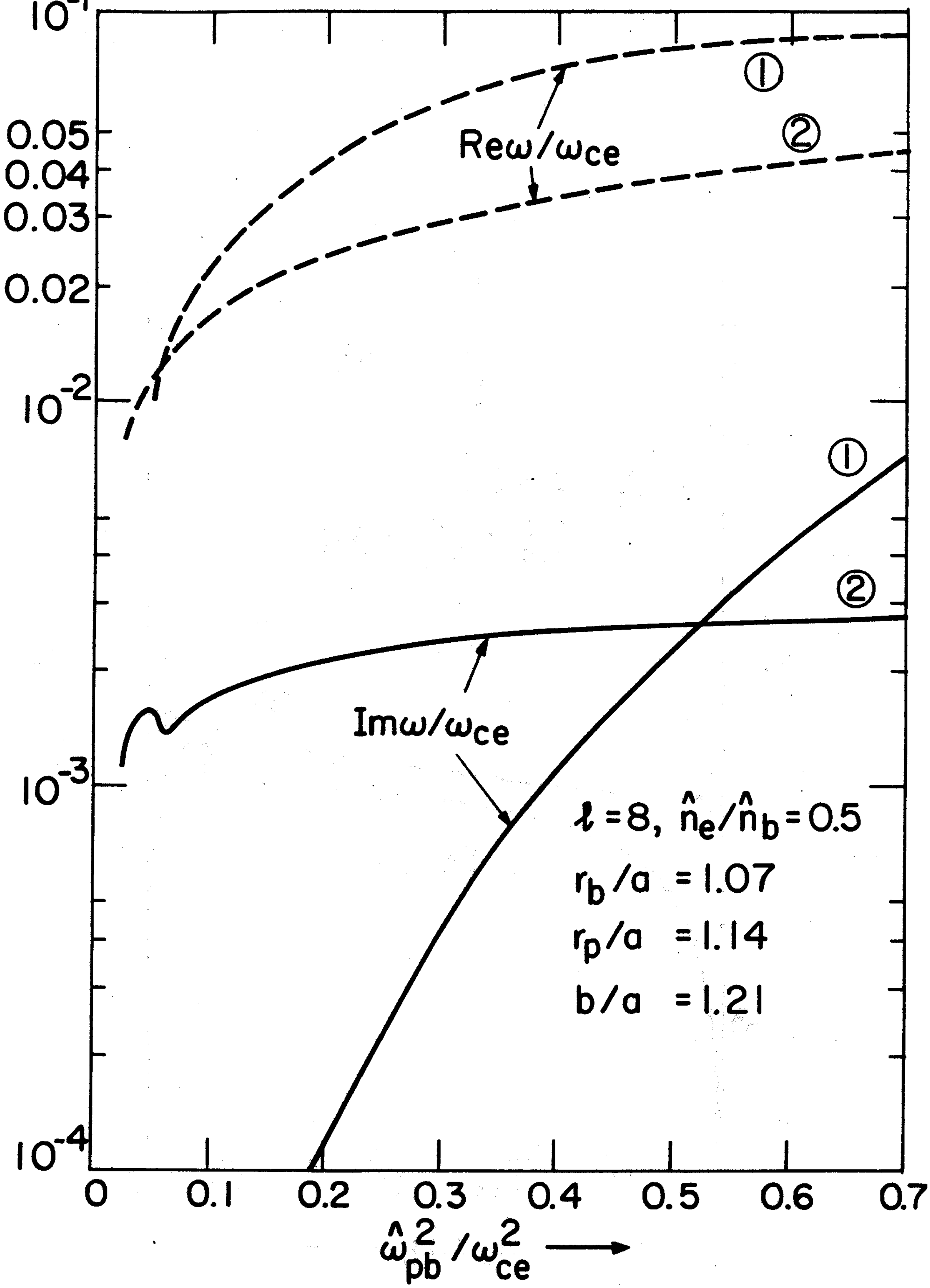
10^{-1}
0.05
0.04
0.03
0.02
10^{-2}
10^{-3}
10^{-4}
0
0.1
0.2
0.3
0.4
0.5
0.6
0.7
$\hat{\omega}_{pb}^2/\omega_{ce}^2$ →
$\mathrm{Re}\,\omega/\omega_{ce}$
$\mathrm{Im}\,\omega/\omega_{ce}$
①
②
①
②
$\ell = 8$, $\hat{n}_e/\hat{n}_b = 0.5$
$r_b/a = 1.07$
$r_p/a = 1.14$
$b/a = 1.21$

Fig. 14

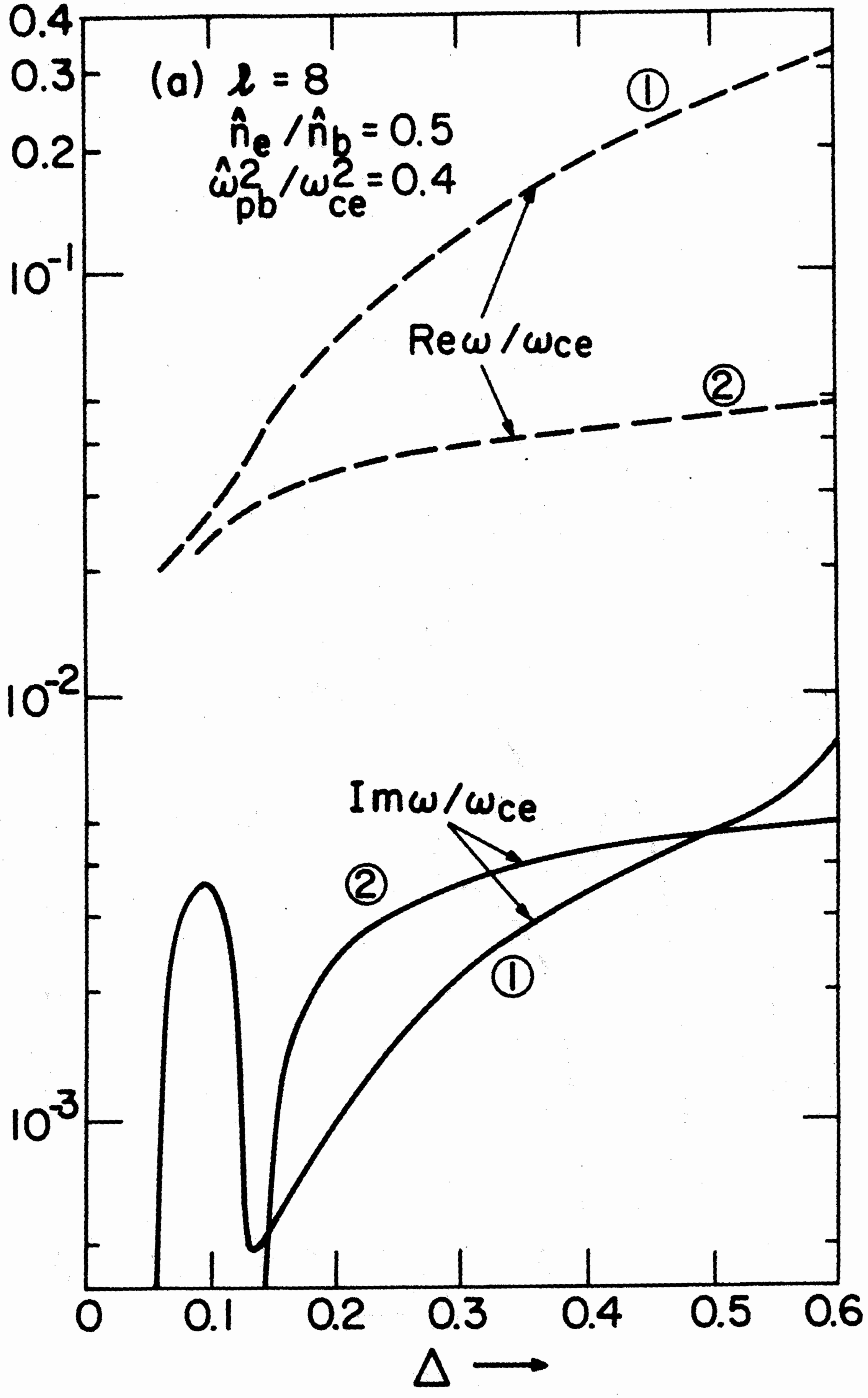
(a) $\ell = 8$
$\hat{n}_e/\hat{n}_b = 0.5$
$\hat{\omega}_{pb}^2/\omega_{ce}^2 = 0.4$
①
②
$Re\omega/\omega_{ce}$
$Im\omega/\omega_{ce}$
②
①
0.4
0.3
0.2
10^{-1}
10^{-2}
10^{-3}
0
0.1
0.2
0.3
0.4
0.5
0.6
$\Delta \rightarrow$

Fig. 15(a)

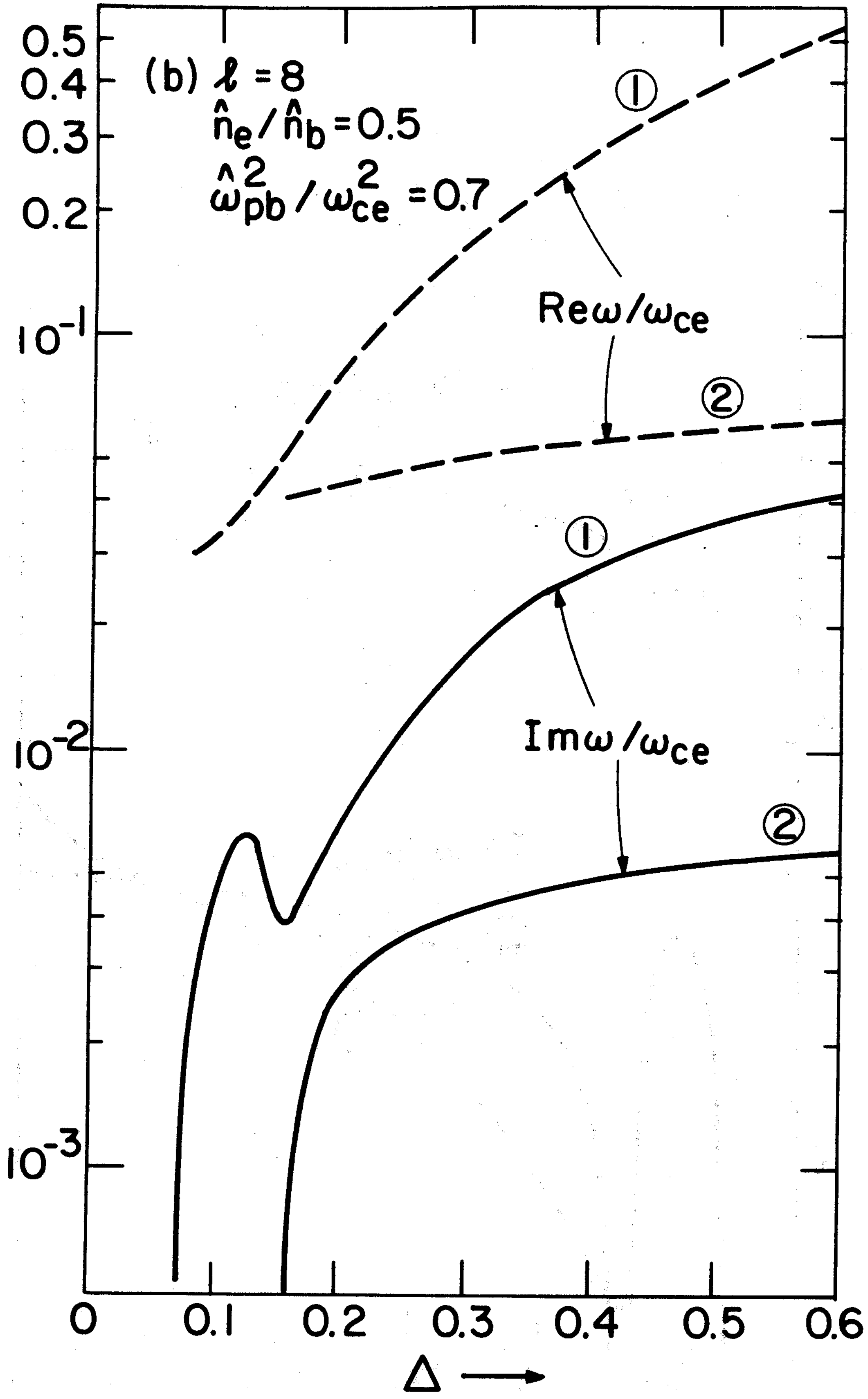
(b) $\ell = 8$
$\hat{n}_e/\hat{n}_b = 0.5$
$\hat{\omega}_{pb}^2/\omega_{ce}^2 = 0.7$
$\mathrm{Re}\,\omega/\omega_{ce}$
$\mathrm{Im}\,\omega/\omega_{ce}$
①
②
①
②
0.5
0.4
0.3
0.2
10^{-1}
10^{-2}
10^{-3}
0
0.1
0.2
0.3
0.4
0.5
0.6
$\Delta \rightarrow$

Fig. 15(b)